



UNIVERSIDAD
NACIONAL
DE COLOMBIA
—
SEDE BOGOTÁ
FACULTAD DE CIENCIAS



STUDY OF THE EXCESS IN WHITE-LIGHT DURING SOLAR FLARES VIA THE BACKWARMING MODEL.

UNDERGRADUATE FINAL YEAR PROJECT
SUBMITTED TO
UNIVERSIDAD NACIONAL DE COLOMBIA
AS PARTIAL REQUISITE TO OBTAIN THE B.SC. DEGREE IN PHYSICS
FACULTAD DE CIENCIAS

JUAN SEBASTIÁN CASTELLANOS DURÁN

Advisor: Benjamín Calvo-Mozo

Observatorio Astronómico Nacional

External advisor: Juan Carlos Martínez Oliveros

Space Sciences Laboratory - University of California, Berkeley

PHYSICS DEPARTMENT AND OBSERVATORIO ASTRONÓMICO NACIONAL
UNIVERSIDAD NACIONAL DE COLOMBIA
2014



UNIVERSIDAD
NACIONAL
DE COLOMBIA
—
SEDE BOGOTÁ
FACULTAD DE CIENCIAS



ESTUDIO DEL EXCESO EN EMISIÓN DE LUZ BLANCA
DURANTE FULGURACIONES SOLARES POR MEDIO DE
MODELO BACKWARMING.

TRABAJO DE GRADO
CARRERA DE FÍSICA
UNIVERSIDAD NACIONAL DE COLOMBIA
FACULTAD DE CIENCIAS

JUAN SEBASTIÁN CASTELLANOS DURÁN

Director: Benjamín Calvo-Mozo

Observatorio Astronómico Nacional

Asesor: Juan Carlos Martínez Oliveros

Space Sciences Laboratory - University of California, Berkeley

DEPARTAMENTO DE FÍSICA Y OBSERVATORIO ASTRONÓMICO NACIONAL
UNIVERSIDAD NACIONAL DE COLOMBIA
2014

CONTENTS

List of Figures	III
List of Tables	V
Abstract	VI
Acknowledgements	VII
Abbreviations	VIII
1 Introduction	1
1.1 The Sun	1
1.2 Solar Flares	5
1.2.1 Classification	7
1.2.2 The standard solar flare model	8
1.2.3 White light during solar flares	8
2 Theory and model initial conditions of the atmosphere during flares	9
2.1 Brief introduction to white-light flares models	9
2.2 Radiative transfer	11
2.3 Line formation	14
2.4 The backwarming model	15
2.5 Heating/cooling functions	16
2.6 Energy transport under the Backwarming model	18
2.7 The solar atmosphere model during flares:	
Initial conditions	19
2.7.1 Flare-atmosphere models	19
2.7.2 H ⁻ opacity	20
2.7.3 Hydrogen, Silicon and Carbon opacities	21

3 Observations	24
3.1 Solar Dynamics Observatory: Helioseismic and Magnetic Imager	24
3.1.1 Data set	25
3.2 Differences and mask methods	26
3.3 Differences methods	36
3.3.1 Normal and mean-differences methods	36
3.3.2 Integration-differences method	38
3.3.3 Masks	40
4 Discussion	42
4.1 Atmospheric model results	42
4.2 Observational results	44
4.3 Summary	49
5 Bibliography	54
A Attended conferences, papers & posters.	60

LIST OF FIGURES

1.1	Solar structure	3
1.2	The solar photosphere, chromosphere and corona.	4
1.3	Solar flare phases	6
2.1	Machado, Emslie, and Avrett (1989) intensities results during a flare	16
2.2	The net radiative cooling/heating rate from Machado <i>et al.</i> (1980)	17
2.3	The VAL-C numerical densities of the hydrogen n_H , electron n_e and H^- numerical density.	19
2.4	Grotian diagrams of Silicon (<i>left</i>) and Carbon	21
3.1	The Solar Dynamics Observatory and the Helioseismic and Magnetic Imager instrument	24
3.2	White-light flare sample	26
3.3	Normal-differences of flare SOL-2011-07-30T02:12.0.	28
3.4	Mean-differences of flare SOL-2011-07-30T02:12.0.	29
3.5	Integration-differences of flare SOL-2011-07-30T02:12.0.	30
3.6	Reconstructed images of flare SOL-2011-07-30T02:12.0.	31
3.7	Normal-differences of flare SOL-2011-09-06T22:20.0.	32
3.8	Mean-differences of flare SOL-2011-09-06T22:20.0.	33
3.9	Integration-differences of flare SOL-2011-09-06T22:20.0.	34
3.10	Reconstructed images of flare SOL-2011-09-06T22:20.0.	35
3.11	Comparison between differences methods using the one pixel light-curve . .	37
3.12	Cartoon of a solar flare signal	38
3.13	Flare's signal reconstruction algorithm for integration-difference method. .	39
3.14	Intensity mask and photometric mask.	41
4.1	Temperatures and H^- density profiles throughout solar atmosphere where hight densities mean lower slabs.	42
4.2	Opacities	43

4.3	Net radiated cooling rate for flare conditions.	44
4.4	White light emission at flare's peak observed by SDO/HMI	45
4.5	GOES-class (W m^{-2}) versus total WL energy emitted at 6173 Å using the integration method	48
4.6	WL enhancement curve using the mean-differences method during flare SOL-2011-07-30T02:12.0	50
4.7	WL enhancement curve using the integration-differences method during flare SOL-2011-07-30T02:12.0	51

LIST OF TABLES

1.1	General data of the Sun	2
1.2	Type of energies and their common values in solar atmosphere.	5
1.3	GOES Classification for Solar flares	7
1.4	Soft X-rays light curves observed by GOES during two days on February 2011	7
2.1	Atomic data of our H, Si and C eighth energy levels model	23
3.1	Set of flares that were analyzed	25
4.1	General information of 27 White-light flares observed on the current solar maximum	52
4.2	WL intensity at 6173 Å, its area and total energy emitted during 27 WLs observed on the current solar maximum.	53

ABSTRACT

We present an analysis of the white-light emission during flares which is an unknown puzzle on the understanding of this events. On the introductory chapter it is illustrated the solar interior and its atmosphere structure and features. In addition on this chapter we present an overview of solar flare, their classification, semi-empirical model and relevant observational results of white-light flares.

On chapter two we list some of the most important models to explain the excess on the continuum intensity and it is explained in detail the Backwarming model (Machado, Emslie, and Avrett, 1989) which is the model chosen to perform our numerical calculations. On the same chapter we discuss the basic concepts of the radiative transfer theory, line formation and net radiated rates which show the dissipation or production of energy in a medium. We conclude chapter two presenting the chosen atmospheric initial conditions and with an explanation of the negative hydrogen ion and the atomic model performed (Vernazza, Avrett, and Loeser, 1973, 1976, 1981).

Chapter three presents the data set chosen from SDO/HMI instrument and a discussion of the reduction methods to achieved the white-light excess measurements during flares. We end this work discussing our observational and numerical results as well as a summary of the work.

ACKNOWLEDGMENTS

I would like to dedicate this work to many people that directly or indirectly have contributed to develop this accomplishment. I want to show my gratitude to my advisor Benjamín Calvo-Mozo, I have been working with him for the last three years and at this time, I have to say that this world is a better place thanks to wise people like him. I have not only become a better physics and astronomer, but also a better person because of all the life lessons learnt from him. It is also very important to acknowledge to Juan Carlos Martínez Oliveros for all of our academic discussions. One-by-one, they achieved better results in my work and they gave me a deeper knowledge about solar physics. I cannot forget to thank all the members of the Solar astrophysics group and in special to Julian D. Alvarado-Gómez and Wilmar Fajardo because with them the classical expression of team work has become true. I would also like to acknowledge the English corrections made by Martha Castellanos Obregón. Finally, I must put into words my appreciation to my amazing friends, family, professors, mentors, sister, brothers, Isabella and in particular to my wonderful mother Patricia and father Juan. For all this people; there are not enough words to express my gratitude to them and I just can say thank you.

ABBREVIATIONS

- AIA Atmospheric Imaging Assembly, 25
CNES Centre national d'études spatiales, 3
CNO Carbon-Nitrogen-Oxygen cycle, 1
EUV Extreme Ultra Violet, 6
EVE Extreme Ultraviolet Variability Experiment, 25
GOES Geostationary Operational Environmental Satellites, 7
HMI Helioseismic and Magnetic Imager, 25
HXR Hard X-rays, 8
LTE Local Thermodynamic Equilibrium, 3
MEB Flare atmospheric model by (Machado, Emslie, and Brown, 1978), 19
PP Proton-Proton chain, 1
RHESSI Reuven Ramaty High Energy Solar Spectroscopic Imager, 26
RTE Radiative Transfer Equation, 11
SDO Solar Dynamics Observatory, 25
SORCE SOlar Radiation and Climate Experiment, 47
SSW SolarSoftWare, 26
SXR Soft X-rays, 6
TIM Total Irradiance Monitor, 47
VAL-C Quiet-sun atmospheric model by Vernazza, Avrett, and Loeser (1981), 19
WLF White-Light Flare, 8
XUV X-rays and ultraviolet irradiation, 18

In memoriam

Beatriz Obregón de Castellanos

A tus hermosas sonrisas, historias y enseñanzas.

*Por todos aquellos momentos
que deleitamos tus recetas y bella compañía.*

CHAPTER
ONE

INTRODUCTION

This chapter presents some general topics about the Sun such as the solar structure, its internal and atmospheric processes and energy transport mechanisms through each layer. Additionally, it presents how flares are classify by their radiated power, the semi-empirical standard solar flare model and some of its semi-empirical results like the magnetic reconnection, the Neupert effect. The last part of the chapter points out what is a white-light flare and the observational results of this kind of events.

1.1 The Sun

The Sun is the closest star from the Earth. The Sun is in hydrodynamic equilibrium which means that it is in the main sequence with an spectral class of G2V. The distance from the Earth between the Sun is approximately 150 million kilometers or 8 light-minutes. It orbits around the center of the Milky Way with a mean speed of $\sim 220 \text{ km s}^{-1}$. Its mass and its radius are $\sim 335,000$ and ~ 107 times Earth's mass and radius respectively. Some general information about the Sun are shown in the table 1.1.

One can characterize the solar interior and its atmosphere as a combination of different regions. Each layer is defined by a physical process that regulates the energy transport therein. The deepest region is *the core* which produces energy due to fusion processes. The Proton-Proton chain (PP) is the dominant nucleosynthesis process in the core, however, some energy is generate by the Carbon-Nitrogen-Oxygen (CNO) cycle which is important in mixing. In a distance of $\approx 0.25R_{\odot}$ the whole energy by fusion mechanisms have been produced, then, the energy begins to be transported by thermal radiation until the $\approx 0.69R_{\odot}$ of solar radius, this layer is called *the radiative zone*.

Continue going out through the solar interior, one finds the *tachocline* centered at $\sim r_{tacho} = 0.693 \pm 0.003 R_\odot$ (Miesch, 2005). This interface region the Sun begins to rotate differentially, i.e. the speed of rotation at latitudes close to the equator are faster, with a period of rotation equals to 25 days. However, at those latitudes near to the poles the period of rotation is 30 days. The last zone of solar interior is between from $r_{conv} = 0.0713 \pm 0.003 R_\odot$ to the photosphere. This region is called *the convection zone* because the energy is transported by this kind of processes (see figure 1.1). The last two layers are so important on the behavior of “solar activity” because in the tachocline and the convection zone, it is thought that the solar magnetic field are generated by dynamo processes (Hughes, Rosner, and Weiss, 2007; Charbonneau, 2010; Miesch, 2005).

Physical parameter	Symbol	Value
Mass	M_\odot	$1.989 \times 10^{30} \text{kg}$
Ratio	R_\odot	$6.960 \times 10^8 \text{m}$
Mean density	$\bar{\rho}$	1409kg m^{-3}
Central density	ρ_c	$1.6 \times 10^5 \text{kg m}^{-3}$
Luminosity	L_\odot	$3.9 \times 10^{26} \text{W}$
Effective temperature	T_e	5785K
Central temperature	T_c	$1.5 \times 10^7 \text{K}$
Absolute visual magnitude	M_V	4.79
Spectral class		G2V
Surface chemical composition	X	0.71
	Y	0.27
	Z	0.02

Table 1.1: General data of the Sun (Karttunen *et al.*, 2007).

The *photosphere* is the first layer of solar atmosphere that is directly observed (Zirin, 1966). This zone is known as the “surface” of the Sun and it is said that photosphere starts when the optical depth (τ_ν) at 5000 Å equals one. In this zone can be observed different kind of effects or structures e.g. granulation (convection lattices), faculae, sunspots and bright points over this surface (see figure 1.2, top). Sunspots are produced by the solar magnetic field lines emerging from the solar interior which inhibit energy transport by convection. Then, the intensity in a sunspot is $\sim 77\%$ less than the photosphere’s intensity. The temperature on sunspots is the order of

$$T_{spot} = (3950 \pm 150) \text{K} \quad T_{phot} = (5780 \pm 15) \text{K} \quad (1.1.1)$$

In addition, sunspots are characterized by a dark core, umbra, less dark halo and penumbra. On the umbra the magnetic field is stronger (2000 - 3700 G) and lines more oriented

in the perpendicular direction to the surface. On the other hand, over the penumbra the inclination of the magnetic lines become stronger producing a decrement on the magnetic field (Solanki, 2003), see figure 1.2, top-right and middle-right. At this point a following important remark must be made; on the study of solar flares, the sunspots or active regions are very important because they host most of flares.

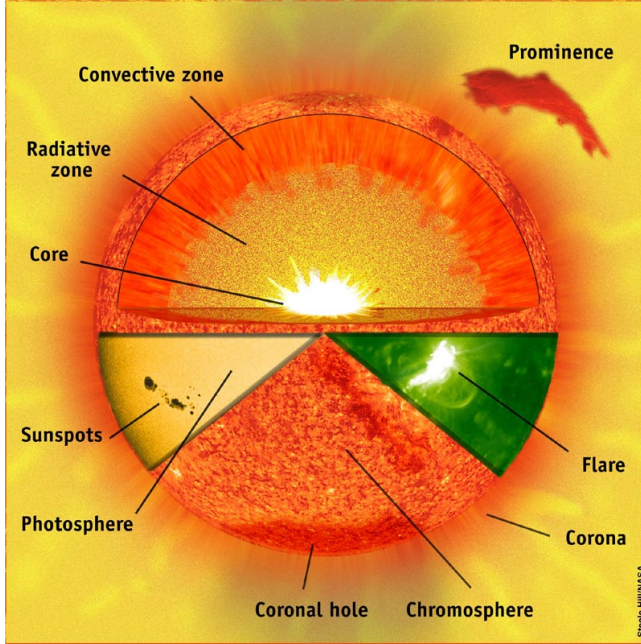


Figure 1.1: Solar structure. Credits: Centre national d'études spatiales (CNES).

Going upper along the solar atmosphere we find the *chromosphere*. On this region is located the temperature-minimum region of the whole solar atmosphere, and other phenomena known as spicules (De Pontieu, Erdélyi, and James, 2004; de Pontieu *et al.*, 2007) and plages (Hale and Ellerman, 1904) (figure 1.2, bottom-left). It is important to point out that chromosphere is not in Local Thermodynamic Equilibrium (LTE), therefore, emission lines are produced at this zone. For the purpose of this work it will be continuously referring to the chromosphere because if one can heat it to a temperature of 10^4K , then, the lower layers of solar atmosphere will have an enhancement on white light.

Lastly, the *transition region* is the connection between the chromosphere and the corona (detailed below). Along this region there is a strong gradient on temperature from $\sim 10^3\text{K}$ to $\sim 10^6\text{K}$. However, the density behaves on the opposite way, i.e. it decreases from the chromosphere to the corona. The reason to explain this phenomenon is still open, and it is known as the *coronal heating problem*. Thus, the next layer of the solar atmosphere known as *corona* goes from the transition region and then gets combined with the *Solar Wind* (Bruno and Carbone, 2013) and *Space Weather* (Pulkkinen, 2007) beyond Pluto's orbit. The lines produced in the corona are highly ionized, meaning high temperatures in this region. Now, an example of how the solar corona looks like is on figure 1.2, bottom-right. That image is a AIA 3-color composition of the channels at 211 Å (Fe XV, 2MK), 193 Å (Fe XII, 1.5MK) and 171 Å (Fe IX/X).

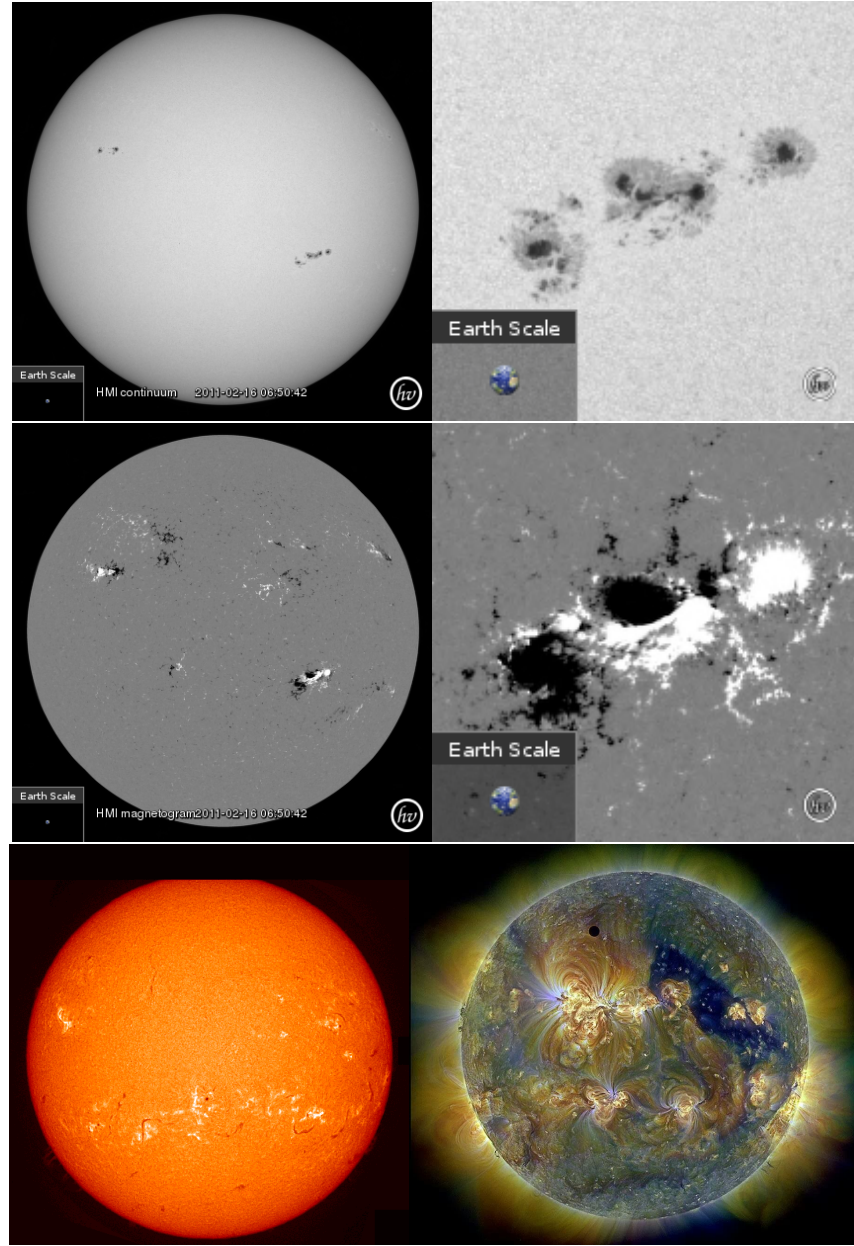


Figure 1.2: The upper images show the solar photosphere observed by SDO/HMI at 6173 Å. The middle images are plotted the magnetic field on the line-of-sight over the photosphere. We present this images from www.helioviewer.org to give an idea of how big is the Sun comparing with Earth's size. The bottom left image presents chromosphere observed at the Kanzelhoehe Solar Observatory (Austria). The bottom right figure shows a composition image of three channels observing the solar corona. Those images were taken by the Atmospheric Imaging Assembly (AIA) on board SDO.

1.2 Solar Flares

Solar flares are explosive events that are characterized by brightness increase in the whole electromagnetic spectrum, i.e. they present emission in optical- and radio- wavelengths, generation of X-rays, γ -rays and also show movements of vast amount of solar mass. It is believed that the first solar flare was observed independently by R.C. Carrington and R. Hodgson on September 1st, 1859. The word flare was first introduced by Bartels in 1932, but this term started to be used by Richardson in 1944 (Benz, 2008). Richardson said:

“...The strongest reason for the adoption of ‘flare’ is that in one word are combined the most outstanding features of the phenomenon: its sudden appearance, great brilliancy, and rapid variations in intensity...” (Richardson, 1944)

Nowadays, solar flares are defined as explosive processes in the solar atmosphere due to the sudden release of magnetic energy. Along these lines, the physical mechanism is known as *magnetic reconnection*. In addition, one would be able to define flares as a sudden emission in some bands of the electromagnetic spectrum and with a time scale of minutes (Benz, 2008). The common conditions to generate a solar flare are

$$\left. \begin{array}{l} E \sim 10^{32} \text{erg} \\ V \sim d^3 \sim 10^{30} \text{cm}^3 \end{array} \right\} \quad \rho_E \sim 100 \text{ erg cm}^{-3} \quad (1.2.1)$$

where E is the energy, V volume in which the flare is produced, and ρ_E is the energy density to generate those events.

Due to the large amount of energy that is necessary to produce a solar flare neither the kinetic, nor thermal, nor gravitational energy are capable to generate it. Consequently, the only physical process able to store enough energy to generate those events is the magnetic field (see table 1.2).

Energy form	Mean observational values	Energy density [erg cm ⁻³]
Kinetic $n \frac{m_p v^2}{2}$	$n = 10^9 \text{cm}^{-3}$, $v = 10 \text{km s}^{-1}$	$\sim 10^{-3}$
Thermal $n k_B t$	$T = 10^6 \text{K}$	$\sim 10^{-1}$
Gravitational $m_p h g$	$h = 10^5 \text{km}$	$\sim 4 \times 10^{-1}$
Magnetic $\frac{B^2}{8\pi}$	$ \vec{B} = 100 \text{G}$	~ 400

Table 1.2: Type of energies and their common values in solar atmosphere.

Historically flares have been characterized in phases as consequence of some observational results such as: preflare, impulsive, flash and decay phase. A particular phase is associated to the emission process(es) in each different band all over the electromagnetic spectrum (see figure 1.3).

The preflare phase has been observed since 1959 (Bumba and Křivský, 1959). It has a time range of some minutes where coronal plasma starts heating and after emitting in Soft X-rays (SXRs) and in the Extreme Ultra Violet (EUV).

Kane and Donnelly (1971) introduced the term of impulsive phase which has a duration of $\sim 3 - 10$ minutes. On this phase occurs a fast energy conversion from coronal magnetic fields by reconfigurations and relaxation of their lines. Thus, at the end of the impulsive phase SXR arises to its maximum. This phase is very important on this work because the white-light enhancement take place in there.

Athay and Moreton (1961) defined flash phase as a period with an abrupt increment in the flare brightness. This increment is observed as a fast emission in H α , when it arrives to its peak. Finally, during the delay phase the solar atmospheric plasma slowly returns to its original state.

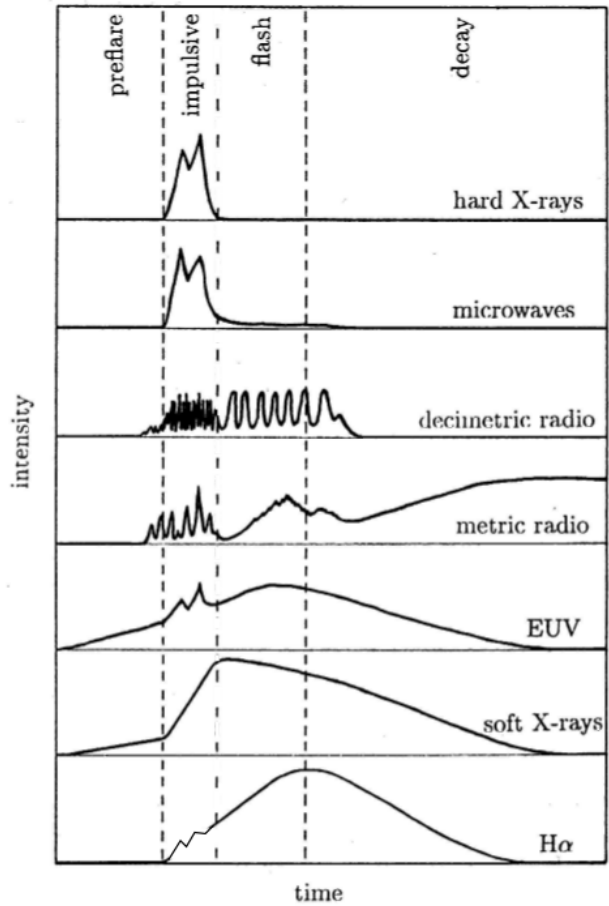


Figure 1.3: Solar flare phases (Benz, 2000).

1.2.1 Classification

GOES Class	Peak on 1 to 8 Å [Wm ⁻²]
A	$I_f \leq 10^{-7}$
B	$10^{-7}I_f < 10^{-6}$
C	$10^{-6}I_f < 10^{-5}$
M	$10^{-5}I_f < 10^{-4}$
X	$I_f \geq 10^{-4}$

Table 1.3: GOES Classification for Solar flares, where I_f is the flux per unit area in SXR.

One can classify flares in too many ways; one of the most used is the logarithm classification based on the soft X-ray flux measured with the Geostationary Operational Environmental Satellites (GOES). This satellite measures the SXR flux (W m^{-2}) with a passband from 0.5 to 4.0 Å and from 1.0 to 8.0 Å. This classification consists of taking each peak of SXR light-curves at 1.0 to 8.0 Å (see figure 1.4), so each peak implies a flare. Hence, the flux of a peak is assigned to the letters A, B, C, M and X ; being A the weakest

and X the most powerful class. For example, a flare X1.8 represents a flux of $1.8 \times 10^{-4} \text{ W m}^{-2}$ (see table 1.3). To have an idea how strong can be a solar flare, one has to consider that the energy released during a medium M-class event is $\approx 5 \times 10^{27} \text{ ergs}$, i.e. approximately the annual global energy consumption.

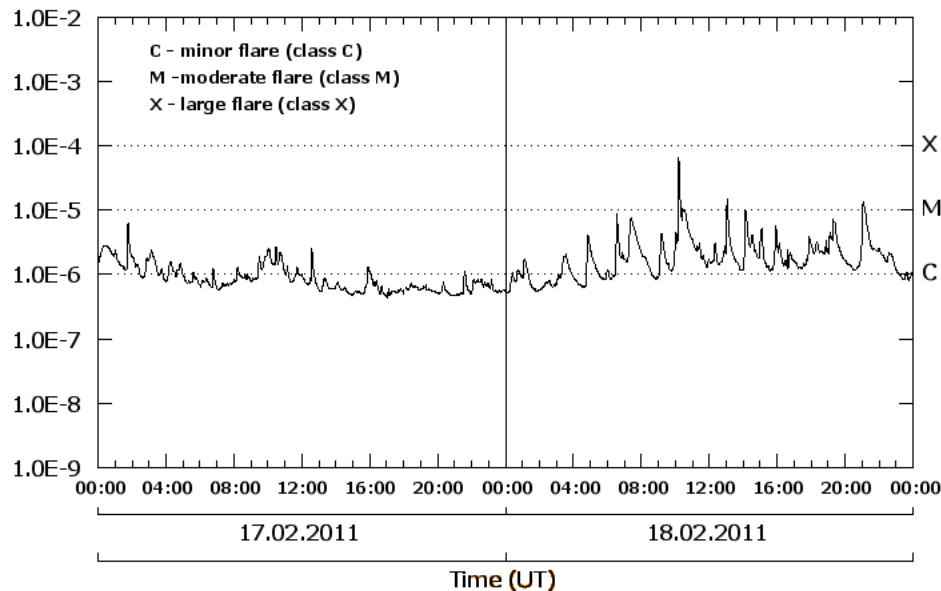


Table 1.4: Soft X-rays light curves observed by GOES during two days on February 2011. From <http://www.thesis.lebedev.ru/en>

1.2.2 The standard solar flare model

This semi-empirical model postulates that the energy released during flares somehow accelerate particles, which later interact with some material generating the observed X-ray emission. However, this model does not explain the acceleration mechanism; the standard model describes of the observational phenomena along solar flares, such as, the Neupert effect¹, the location of the sources of Hard X-rays (HXR), the tendency of thermal energy contained in soft X-ray source is smaller than the energy in accelerated electrons, the chromospheric evaporation, (Antonucci, 1989), among others .

1.2.3 White light during solar flares

In particular, some solar flares present an enhancement in white-light emission, as was shown by Carrington in 1859. Therefore, those special events are called White-Light Flare (WLF) because of their excess in white light (WL).

The theoretical and observational understanding of WLF has improved on the last decades (for an overview of these theoretical approaches see §2.1). Although, the instrumental limitations have not permitted to achieve a possible statistical correlation WLFs with other physical parameters, there are different observational approaches to investigate the WLF phenomenon. One of these results have proposed a classification in two types of WLF based on the presence of spectral features such as Balmer and Paschen jumps and WL continuum - X-rays - microwave correlations (Machado *et al.*, 1986; Fang and Ding, 1995; Ding, Fang, and Yun, 1999). Moreover, several observational studies have pointed out some correlation between WL - HXR to include timing (Neidig and Kane, 1993; Hudson *et al.*, 1992), their relative horizontal positions (Metcalf *et al.*, 2003; Matthews *et al.*, 2003; Hudson, Wolfson, and Metcalf, 2006; Fletcher *et al.*, 2007) and their height (Martínez Oliveros *et al.*, 2012; Battaglia and Kontar, 2011).

In this work, we carry out an analysis of white-light-flare emission by model and observational approaches. On chapter 2 we describe the necessary background concepts of the radiative emission and transport throughout stellar atmospheres and an idealized model of how is heated lower layers of solar atmosphere known as the Backwarming process. On chapter 3 we present the data observations used and the reduction applied on HMI/continuum images. We end on chapter 4 with an analysis of our results and summary.

¹This effect shows the time correlation between the emission of soft X-rays ($F_{SX R}(t)$) and the accumulation of hard X-rays ($F_{HXR}(t)$), known as the *Neupert effect*

$$F_{SX R}(t) \propto \int_{t_0}^t F_{HXR}(t') dt' \quad (1.2.2)$$

CHAPTER
TWO

THEORY AND MODEL INITIAL CONDITIONS OF THE ATMOSPHERE DURING FLARES

In this chapter we point out some theoretical topics that are important when we are dealing with white-light emission. We begin a brief introduction of some models that have been proposed in the last decades (§ 2.1). After that, we present some basic concepts of radiative energy transport, such as intensity, flux, source function and the radiative transfer equation (§ 2.2).

Thenceforth, we focus the discussion on the Backwarming model as proposed by Machado, Emslie, and Avrett (1989) to develop our numerical model (§ 2.4). The objective of this model is to consider the emission process(es) to overheat the lower layers and the transport processes of flare's energy throughout solar atmosphere (§ 2.6). On the other hand, we introduce some topics that are important for our model such as the line emission (§ 2.3) and heating/cooling function (§ 2.5). Finally we present the initial conditions of the solar atmosphere during a flare.

2.1 Brief introduction to white-light flares models

The white light emission during a solar flare has been studied on an observational basis with different instruments and techniques. These kind of events have been dated for a long time, e.g., Hudson *et al.* (1992); Fletcher *et al.* (2007); Metcalf *et al.* (2003); Rust (1986); Martínez Oliveros *et al.* (2011); Battaglia and Kontar (2011); Donnelly (1976); Matthews *et al.* (2003). From this phenomenological behaviour several theoretical scenarios have been proposed, for instance (Aboudarham and Henoux, 1986; Allred *et al.*, 2005; Hudson, 1972; Machado, Emslie, and Avrett, 1989)

It is known that the white-light excess is produced in the impulsive phase, and it is already known that an emission of this type of radiation during a flare, have a spatial and

temporal correlation with the non-thermal X-rays (see § 1.2.3). Additionally, there is a huge debate around the question: *Do all flares have an enhancement in the continuum?* (Jess *et al.*, 2008). Therefore, before answering this question, we keep working with facts coming directly from observations:

There are some flares that have a strong excess in white-light (thereafter White-Light Flares), and there are other flares that do not present any kind of excess.

In such a way, the white-light flares challenge the solar community in different aspects, for example, there is no agreement about which one, out of various models, explains the white-light emission process and its transport throughout solar atmosphere.

The most renowned models that try to explain the excess in white-light during a flare, are:

- i) The overionization over chromosphere (Hudson, 1972; Aboudarham and Henoux, 1986).
- ii) The heating process on layers, such as, around the minimum of temperature, the lower chromosphere and the photosphere, due to that radiation that was produced on upper layers by the flare processes. This model is known as the *Backwarming* model (Machado, Emslie, and Avrett, 1989).
- iii) The process of losing energy by protons (Najita and Orrall, 1970; Zharkova and Kobylin-skii, 1993).
- iv) The thin-target model (Unsold, 1968).
- v) The hydrodynamic radiation model (Allred *et al.*, 2005).

For all of the above reasons, it is an imperative objective on solar physics to be able to discriminate which of those models provide (or emit in-situ) enough amount of energy to the solar-atmosphere plasma to achieve the flare's temperatures (either the upper photosphere or the chromosphere) and consequently, to produce an excess in white-light.

Thus, this work approaches in two ways of the white-light flare problem. First, we perform a 1D model of radiative transfer throughout solar atmosphere based on the Machado, Emslie, and Avrett (1989)'s model. Then, we take those results and compare them with some observations made by SDO/HMI instrument (see chapter 3). However, before we introduce in detail the backwarming model, we present the radiative transfer theory.

2.2 Radiative transfer

The main idea of a stellar atmosphere model is to solve the equation that describes how the radiation is transferred throughout the atmosphere. Henceforth, this section explains its basic form and some of its characteristics. As a result, we will do have a form of the Radiative Transfer Equation (RTE) that describes the energy transport by photons. This equation is going to be solved numerically, taking into account the backwarming process during a flare over solar atmosphere (see section 2.7). The next discussion is based on Chandrasekhar and Chandrasekhar (1967); Emerson (1996).

First of all, we describe two quantities that are essential in astrophysics. Emerson (1996) has defined them as follows:

- i) Intensity I_ν is the energy (E_ν) flow through unit area per unit time (t) per unit solid angle (Ω) and per unit frequencies interval ($\Delta\nu$) with the area perpendicular (a_\perp) to the chosen central direction:

$$I_\nu = \frac{\Delta E_\nu}{\Delta t \Delta a_\perp \Delta \Omega \Delta \nu} \quad (2.2.1)$$

- ii) The flux F_ν is the energy flowing through unit area per unit time and per unit of frequencies interval. Let the solid angle $d\Omega = \sin \theta d\theta d\phi$; then flux and intensity are connected by

$$F_\nu = \int I_\nu \cos \theta d\Omega \quad (2.2.2)$$

Let us write $\mu = \cos \theta$, thus we are able to define other two relevant quantities accordingly to

$$J_\nu = \frac{1}{4\pi} \int I_\nu d\Omega = \frac{1}{2} \int_{-1}^{+1} I_\nu(\mu) d\mu \quad (2.2.3)$$

$$H_\nu = \frac{1}{2} \int_{-1}^{+1} I_\nu(\mu) \mu d\mu \quad (2.2.4)$$

where J_ν is the mean intensity and H_ν is proportional to flux as $F_\nu = 4\pi H_\nu$. The opacity per unit mass κ_ν is the fractional decrease of intensity due to extinction in the given direction, as the cross section of radiation-matter interaction, per unit mass of the propagating medium. Consequently, a large value of opacity indicates a strong absorption of photons by the medium (gas); whereas a small value expresses that the radiation losses very little energy as the beam passes through the medium of density ρ (Rogers and Iglesias, 1994). Then, the opacity change the intensity (dI_ν) over the distance ds as

$$dI_\nu = -\kappa_\nu \rho I_\nu ds \quad (2.2.5)$$

It is customary to define the optical depth τ_ν as a dimensionless quantity, such that the higher its value the stronger the intensity loss along a given direction of some specific radiation for a given medium. Its expression is $d\tau_\nu = \kappa_\nu \rho ds$. Thus, from equation 2.2.5 we have that if one has only extinction the intensity of a radiation beam decreases as $I(\tau_\nu) = I(0)e^{-\tau_\nu}$, where τ_ν is the net optical depth, after the radiation has flowed a length l through the medium:

$$\tau_\nu = \int_0^l \kappa_\nu \rho ds \quad (2.2.6)$$

The optical depth has two cases: if $\tau_\nu \ll 1$ the medium is said to be optically thin and if $\tau_\nu > 1$ the medium is optically thick. We can also express the change of radiation due to extinction as a loss of energy in the given directions as.

$$dE_\nu|_{ext} = -\kappa_\nu I_\nu \rho ds dt da_\perp d\nu d\Omega \quad (2.2.7)$$

If dE_ν is the amount of energy emitted in the frequency interval $(\nu + d\nu)$, in the interval of time (dt) , in the element of solid angle $(d\Omega)$ and per unit of mass of the material, then

$$dE_\nu|_{emi} = j_\nu dm dt d\nu d\Omega \quad (2.2.8)$$

defines the emission coefficient at frequency ν ; we can write dm as $\rho da_\perp ds$. Then, a balance of energy, i.e. energy emitted minus energy extinguished along a given direction, gives:

$$dI_\nu dt da_\perp d\nu d\Omega = j_\nu \rho ds da_\perp dt d\nu d\Omega - \kappa_\nu I_\nu \rho ds dt da_\perp d\nu d\Omega \quad (2.2.9)$$

where dI_ν denotes the net change of specific intensity of a given pencil of radiation. From this energy balance one obtains:

$$dI_\nu = \underbrace{-\kappa_\nu \rho I_\nu ds}_{\text{Absortion}} + \underbrace{j_\nu \rho ds}_{\text{Emission}} \quad (2.2.10)$$

or:

$$\frac{dI_\nu}{ds} = -\kappa_\nu \rho I_\nu + j_\nu \rho \quad (2.2.11)$$

which is known as the equation of radiative transfer. However, dI_ν/ds represents a direction derivative of the specific intensity, for ds sums along the central radiation of some pencil of radiation. So if \hat{n} is a unit vector along that direction, we have that $dI_\nu/ds = \hat{n} \cdot \nabla I_\nu$. Equation 2.2.11 can also be written in terms of the optical depth

$$\frac{dI_\nu}{d\tau_\nu} = I_\nu - S_\nu(\tau_\nu) \quad (2.2.12)$$

where $S_\nu(\tau_\nu)$ is the source function defined as the ratio of the emission coefficient to the absorption coefficient, i.e., $S_\nu(\tau_\nu) = j_\nu / \rho\kappa_\nu$. Let us note that in equation 2.2.12, both I_ν and S_ν are functions of τ_ν . From an observer's point of view, the optical thickness is defined such that at the Sun surface $\tau_\nu = 0$, and its value increases as he sees photons emerging from deeper layers. Thus, in that case:

$$d\tau_\nu = \kappa\rho dl \quad (2.2.13)$$

where dl increases along the visual. Clearly, $dl = -ds$. Then in the observer point of view and on solar analysis, the atmosphere has a thickness of some hundreds of kilometers, thus, if we compare it with its radius, about $R_\odot \approx 7 \times 10^5$ km, one can use the plane-parallel approximation for the equation of radiative transfer that is

$$\mu \frac{dI_\nu}{d\tau_\nu} = I_\nu - S_\nu(\tau_\nu) \quad (2.2.14)$$

Additionally, in Local Thermodynamic Equilibrium (LTE), the source function becomes the Planck's function B_ν given by

$$B_\nu = \frac{2h\nu^3}{c^2} \frac{1}{e^{\frac{h\nu}{k_B T}} - 1} \iff B_\lambda = \frac{2hc^2}{\lambda^5} \frac{1}{e^{\frac{hc}{\lambda k_B T}} - 1} \quad (2.2.15)$$

However, in a more general context, the source function would depend of the radiation field and the gas density. An important point for a model atmosphere is the energy radiative equilibrium. In Emerson's words, this equilibrium can be explained as the emission per unit volume summed over frequency equals to the absorption per unit volume summed over frequency. In mathematically words, it is given by

$$\int_0^\infty j_\nu \rho d\nu = \int_0^\infty \kappa_\nu \rho J_\nu \quad (2.2.16)$$

Now, if we integrate the equation (2.2.14) over θ from $-\pi$ to π , which means for variable $\mu = \cos \theta$ an integration from -1 to 1, we obtained

$$\frac{1}{2} \int_{-1}^{+1} \mu \frac{dI_\nu}{d\tau_\nu} = \frac{1}{2} \int_{-1}^{+1} I_\nu d\nu - \frac{1}{2} \int_{-1}^{+1} S_\nu d\nu \quad (2.2.17)$$

Inverting the integration order, remembering the equation (2.2.4) and assuming that source function is independent of direction, then, we have the basic transfer equation in terms of the mean intensity

$$\frac{dH_\nu}{d\tau_\nu} = J_\nu - S_\nu \quad (2.2.18)$$

2.3 Line formation

An absorption or emission line is produced by three kinds of processes: free-free, free-bound/bound-free and bound-bound. In the absorption case, the free-free process occurs when a free electron absorbs radiation and becomes more more energetic in the presence of a quantum system (atom, ion, molecule). The bound-free or photoionization happens when an electron bound absorbs energy and turns into free state through an excitation of the atom. The bound-bound line absorption occurs when an electron perform a transition from some energy level E_i to E_j being $E_j > E_i$ (excitation). In the emission, the free-free emission is produced when a free electron loss energy going into another free state; this process is also known as Bremsstrahlung process. Free-bound or recombination process is described as the transition to a bound state of a free electron in a certain ionized quantum system. The bound-bound emission process happens when a electron makes a transition from a higher energy E_j to an other lower energy level E_i . A bound-bound transition from a lower energy state to a higher energy one can be done either through an allowed radiation absorption or through a collisional process. Now if the bound.-bound transition goes from a higher energy state to a lower one, radiation can be emitted spontaneously or induce by an external radiation field of the same frequency. The emission of radiation usually occurs when the selection rules hold; in some cases, however there can be also forbidden transitions, when collisional do not compete enough with radiative processes. In many astrophysical contexts we observe forbidden lines due to low particles density, e.g. [OIII] $\lambda 5007$ Å (“hebulium” α), [FeXIV] λ Å (“coronium”).

In present work will take into account for line formation that a fresh sampling atoms act without memory, i.e. atoms emit radiation with no memory of how they were excited. Consequently, the line absorption and emission coefficients have the same frequency dependence (Vernazza, Avrett, and Loeser, 1973; Rutten, 2003). Then, the frequency-independent line source function, S_{ji} , for the transition ji is given by

$$S_{ji} = \frac{2h\nu_{ji}^3/c^2}{(\varpi_j/\varpi_i)(n_i/n_j) - 1} \quad (2.3.1)$$

where ϖ_j and n_j are the statistical weight and the population of the state j , and ν_{ji} is the frequency of the transition ji . Taking into account the Boltzmann equation, one is able to calculate the ratio n_j/n_i as

$$\frac{n_j}{n_i} = \frac{\varpi_j}{\varpi_i} e^{-\frac{h\nu_{ji}}{k_B T}} \quad (2.3.2)$$

In Non-LTE the equation (2.3.1) is re-written in terms of the population departure coefficient b_j accordingly to

$$S_{ji} = \frac{2h\nu_{ji}^3/c^2}{\frac{b_i}{b_j}e^{\frac{h\nu_{ji}}{k_B T}} - 1} \quad (2.3.3)$$

where b_j is defined as

$$b_j = n_j^*/n_j^{LTE} \quad (2.3.4)$$

In addition, the total line extinction coefficient is

$$\alpha_{ji} = \frac{h\nu}{4\pi} (n_j B_{ji} - n_i B_{ij}) \quad (2.3.5)$$

where B_{ji} and B_{ij} are the Einstein coefficient for radiative excitation and deexcitation, respectively.

2.4 The backwarming model

Machado, Emslie, and Avrett (1989) proposed the *Backwarming model*, as a semi-empirical way to overheat the atmosphere and then producing the white-light (WL) observed associated to some flares. Previously, Machado, Emslie, and Brown (1978), Machado *et al.* (1980) developed an atmosphere model during bright and average flares. The backwarming propose that the enhanced white-light continuum emission is produced by (*i*) hydrogen free-bound emission in a heated region in the upper chromosphere, or by (*ii*) H⁻ emission in an enhanced region around the temperature minimum. Furthermore, Machado, Emslie, and Avrett explained that those enhanced regions can be heated by free-photons that are generated during a flare. Those photons can freely travel upwards and downwards through solar atmosphere, so they will be absorbed by the plasma resulting in an increment on the layer's temperature.

In other words, to observe a white-light enhancement is necessary to have enough opacity on the lower layers of the atmosphere to achieve the required brightness over the photosphere background. Hence, Machado, Emslie, and Avrett claimed that the main problem to generate an excess in the continuum emission is reduced to create temperature enhancements of an order of 10⁴ K in the upper chromosphere or 100K around the temperature minimum. Before we mention the reason argued by Machado, Emslie, and Avrett, we introduce the heating/cooling function in next section.

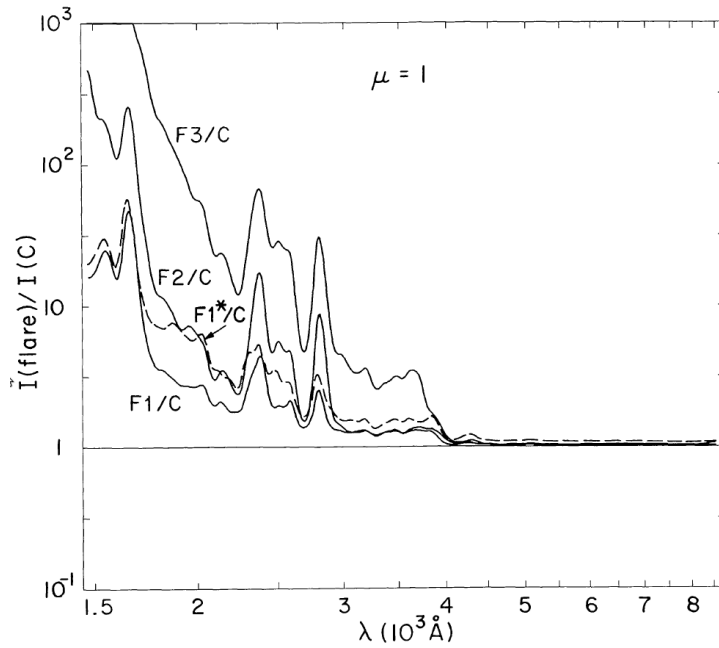


Figure 2.1: Machado, Emslie, and Avrett (1989) intensities results during a flare for the VAL-C quiet Sun C model (Vernazza, Avrett, and Loeser, 1973, 1976, 1981), for MAVN flare models $F1$, $F2$ (Machado *et al.*, 1980), and models $F3$, $F1^*$ proposed by (Machado, Emslie, and Avrett, 1989).

2.5 Heating/cooling functions

The radiated energy rate by a gas is due to the system dissipation or production. This rate can be written in a general form as

$$\frac{dE}{dt} \Big|_{rad} = n_b^2 [\Gamma(T, \dots) - \Lambda(T, \dots)] \quad (2.5.1)$$

where E is the thermal energy of the system, $n_b = n_H + 4n_{He} + \dots$ is the numerical density, Γ is the heating function and Λ is the cooling function. Both functions (Γ and Λ) have the same functional dependency of physical parameters. Henceforth, we can write a function, Ψ , that have the meaning either the heating or cooling function, i.e., the net radiative cooling/heating represents cooling if $\Psi > 0$, or heating if $\Psi < 0$.

$$\left. \begin{array}{l} \Gamma(\dots) \\ \Lambda(\dots) \end{array} \right\} = \Psi(\dots) = \Psi(T, n_b, X_{i,j}, J_\nu) \quad (2.5.2)$$

where $X_{i,j}$ is the abundance of the specie i on the state j (Gnedin and Hollon, 2012). To compute his calculations, Machado, Emslie, and Avrett took the functional form for Ψ given

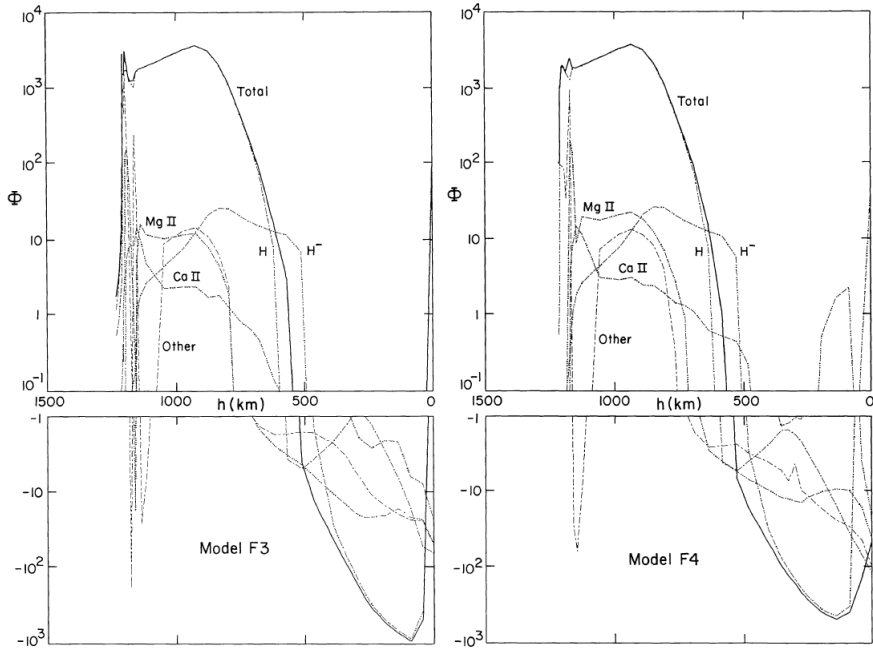


Figure 2.2: Examples of the results from Machado *et al.* (1980). Graphics show the net radiative cooling/heating rate Ψ for two atmosphere models during a flare.

by

$$\Psi = 4\pi \int \kappa_\nu (S_\nu - J_\nu) d\nu \quad (2.5.3)$$

where all terms have the same meaning given in §2.2. An important point is the form of Ψ changes depending on the radiative process, i.e., the heating/cooling function is different for free-free process (bremsstrahlung), free-bound process (recombination), or bound-bound process such as line emission (see Cox and Tucker (1969)). For free-free and free-bound emission by H^- ion during a flare, Aboudarham and Henoux (1986) presented Ψ 's form given by

$$\Psi_{H^-}^{f-f} = 4\pi n_{H^-} \int \kappa_\nu^{f-f} (S_\nu - J_\nu) d\nu \quad (2.5.4)$$

$$\Psi_{H^-}^{f-b} = 4\pi n_{H^-} \int \kappa_\nu^{f-b} \left[\frac{n_{H^-}^*}{n_{H^-}} \left(\frac{2h\nu^3}{c^2} + J_\nu \right) e^{-h\nu/kT} - J_\nu \right] d\nu \quad (2.5.5)$$

where n_{H^-} y $n_{H^-}^*$ are the numerical densities inside and outside the local thermodynamic equilibrium, respectively. Now, recapitulating Machado, Emslie, and Avrett's model, they developed explicit calculations of the transfer equation for H, He, Mg, Ca, Si, Fe, C, and O atoms using the PANDORA code (Avrett and Loeser, 1992). Figures (2.1) and (2.2) show the intensity profiles during a flare from their calculations and the net radiative cooling/heating rates. Consequently, the author suggested that the enhanced white-light continuum emission is due to the sum of H^- and the Balmer continuum from their computed results.

2.6 Energy transport under the Backwarming model

According to the computational results of the Backwarming model, the main point to achieve this radiation field is producing enhancements of order 10^4 K in the chromosphere. Therefore, the radiative output in that region must be the order of 10^3 erg cm $^{-3}$ s $^{-1}$, and the net radiative input into the photosphere should be greater than 10^{10} erg cm $^{-3}$ s $^{-1}$. If these conditions are satisfied the atmosphere will be heated enough to account for the continuum emission. In this way, Machado, Emslie, and Avrett (1989) indicated that there are four possible physical processes to obtain these temperatures. The mechanisms are:

- I) Electron bombardment
- II) Heat conduction
- III) Protons bombardment
- IV) X-rays and ultraviolet irradiation (XUV)

In the electron bombardment mechanism, if we assume a thin-target, we can obtain the amount of energy, which will be deposited on the temperature minimum. This energy is given by $E_{min,e}^2 = \frac{6\pi e^4 \Lambda m_o}{m_H} \approx 170$ keV, where Λ is the Coulomb logarithm and the rest of terms have their typical meaning. To achieve this amount of energy, one would need a huge amount of electron flux that will be too much for normal atmospheric conditions. Thus, electron bombardment is unlike. In the same way, the heat conduction is totally inefficient at temperatures where Balmer continuum is formed.

The proton bombardment was reported by Najita and Orrall (1970). The energy provided by this mechanism over the temperature minimum is $E_{min,p}^2 = \frac{4\pi e^4 \Lambda m_o}{m_e} \approx 6$ MeV. These results imply energies that might be physical observable during a flare. Then, proton bombardment mechanism can be a good candidate to produce the temperature enhancement. Nevertheless, at the time when these models were proposed (1989), there were not strong observational supports for this process.

Finally, we consider the XUV irradiation as a possible mechanism for the overheating around the high chromosphere during a flare; To describe it they used an empirical functional form of the incoming radiation based on Donnelly (1976). In his work, the author (Machado) stated that the XUV field is given by a power law

$$J_\nu(\tau_\nu) = 7.5 \times 10^{-9} \left(\frac{\nu}{10^{17}} \right)^{-1.2} e^{\tau_\nu} \quad \text{erg cm}^{-2} \text{s}^{-1} \text{Hz}^{-1} \text{sr}^{-1} \quad (2.6.1)$$

where all terms have the same meaning described in §2.2. For this work, we assume the XUV irradiation field as the source process to heat the chromosphere.

2.7 The solar atmosphere model during flares: Initial conditions

The numerical part of this work is related to perform a model of the solar atmosphere during a flare using the XUV irradiation field proposed by Machado, Emslie, and Avrett (1989). However, to develop those calculations some initial conditions are necessary such as: temperatures, optical depth, numerical densities, opacities and the atomic data like statistical weights of the electron transitions through the atomic energy levels. Thus, we chose two models for those physical quantities to achieve the numerical calculation and on next subsections they are described.

2.7.1 Flare-atmosphere models

On chapter (1) has been explained that temperature and density change going up on the solar atmosphere. For the purpose of this work, we have chosen the bright and average flare-atmosphere models proposed by Machado *et al.* (1980) (thereafter, MEB model). To compare the flares' conditions, we have selected the extended study of quiet solar atmosphere by Vernazza, Avrett, and Loeser (1973, 1976, 1981) known as the VAL-C model. In figure (2.3) we plot the density and optical depth at $500\mu\text{m}$ profiles of the quiet sun, besides the electron and hydrogen numerical densities of VAL-C and MEB models.

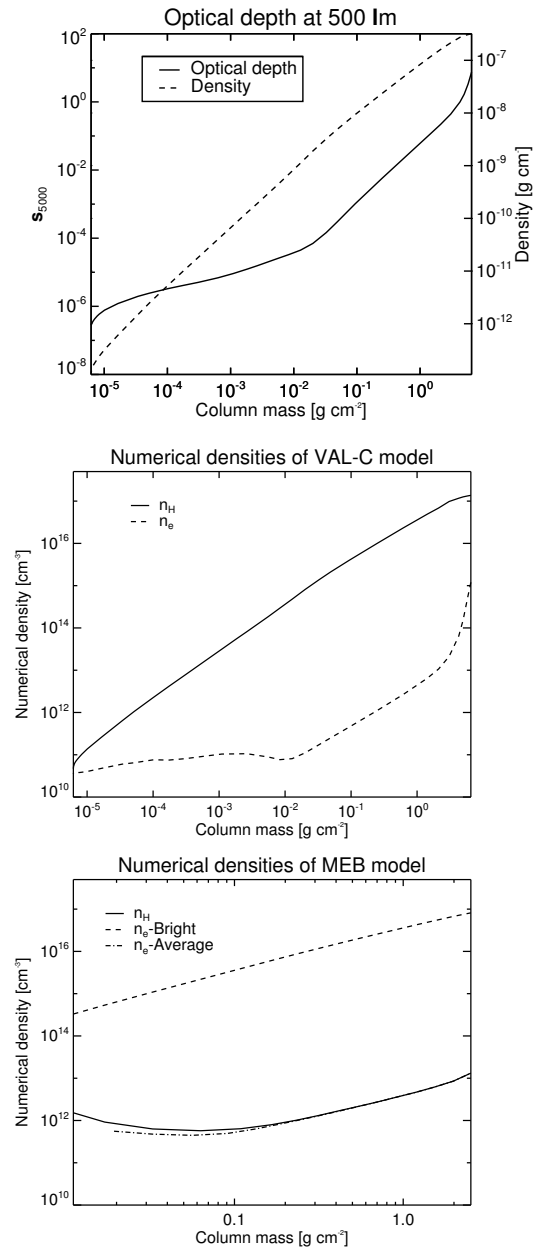


Figure 2.3: Density and optical depth profiles of the quiet Sun (*Top*). Numerical densities of the hydrogen n_H and electron n_e from the VAL-C model (*Middle*) and MEB model (*bottom*).

2.7.2 H⁻ opacity

Not only in the backwarming model but also in atmospheres of cool stars such as the Sun, one of the most important sources of opacity are the free-free and bound-free transitions of the negative hydrogen ion H⁻. Hansen, Kawaler, and Trimble (2004) explain that the reason to produce H⁻ is the large polarizability of the neutral hydrogen atom (HI). This property gives the possibility to attach an extra electron to the HI atom with an ionization potential of 0.75 eV. However, this potential implies that the resulting ion H⁻ is very fragile and will be ionized if temperatures are greater than few thousand degrees. Nonetheless, the generation of H⁻ requires both neutral hydrogen and free electrons. This suggest that any free electron from ionized hydrogen or electrons from outer shell of metals such as Na, K, Ca, or Al will contributed to produce H⁻. Consequently, the opacity of the negative hydrogen ion is sensitive both to temperature and metal abundance. In addition the free-free and free-bound reactions are (Doughty, Fraser, and McEachran, 1966; Doughty and Fraser, 1966)



To calculate the opacities of H⁻, we have followed the Vernazza, Avrett, and Loeser (1976) and Gebbie and Thomas (1970) analysis. The free-bound absorption coefficient is given by

$$\alpha_{H^-}^{f-b}(\nu) = n_{H^-} \sigma(\lambda) \times 10^{-17} \left(1 - \frac{1}{b_{H^-}} e^{-h\nu/kt} \right) \quad (2.7.3)$$

where the opacity and the absorption coefficient are related by $\kappa_\nu = \alpha_\nu / \rho$, and the numerical density is

$$n_{H^-} = 1.0354 \times 10^{-16} b_{H^-} n_e n_{HI} T^{-3/2} e^{8762/T} \quad (2.7.4)$$

being $\sigma(\lambda)$ the cross section (values from Doughty, Fraser, and McEachran (1966)), b_{H^-} the population departure coefficient defined in equation (2.3.4) (Rutten, 2003), finally, n_e , n_{HI} are the electron and neutral hydrogen numerical densities, respectively. On the other hand, the H⁻ free-free opacity came from an analytic approximation to the dipole-length by Stilley and Callaway (1970),

$$\alpha_{H^-}^{f-f}(\nu) = 4.5791 \times 10^{-40} n_e n_{HI} \lambda [1 + 10.631 \lambda (1 - 594.15/T)] \quad (2.7.5)$$

In addition, the negative hydrogen ion and hydrogen free-bound emissivities in unit of ergs s⁻¹ cm⁻³ sr⁻¹ Δν⁻¹ for each mechanism (Hiei, Nakagomi, and Takuma, 1992) can be written

as follows

$$\varepsilon_{\nu}^{H^-} = B_{\nu}(T)\alpha_{H^-}n_{H^-} \quad (2.7.6)$$

$$\varepsilon_{\nu}^{f-b} = 2.15 \times 10^{-32} N^{-3} g^{f-b} n_e^2 T^{-3/2} \exp\left(\frac{\chi_n}{K_B T} - \frac{h\nu}{k_B T}\right) \quad (2.7.7)$$

$$\varepsilon_{\nu}^{f-f} = 5.44 \times 10^{-39} g^{f-f} n_e^2 T^{-1/2} \exp\left(-\frac{h\nu}{k_B T}\right) \quad (2.7.8)$$

where Hydrogen ionization energy is given by $\chi_n = \frac{13.6\text{eV}}{n^2}$, g^{f-b} and g^{f-f} are the Gaunt free-bound and bound-bound coefficients¹

2.7.3 Hydrogen, Silicon and Carbon opacities

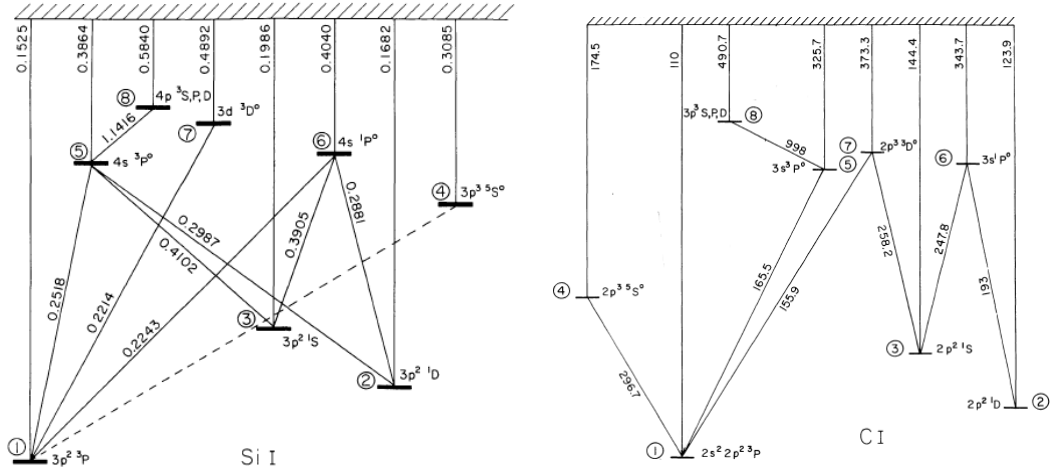


Figure 2.4: Grotrian diagrams of Silicon (left) and Carbon (right) atoms that we have used on the numerical calculations. These diagrams came from Vernazza, Avrett, and Loeser (1976, 1981).

In our atmospheric model we have developed calculations for H, Si and C atoms. The bound-bound hydrogen transition consists on Lyman, Balmer and Paschen spectral series. Also, we simulated the Silicon and Carbon atoms with eight energy levels; their Grotrian diagrams

¹The Gaunt factor g is a quantum correction to the absorption or emission radiation mechanisms. In free-free processes is given by

$$g^{f-f} = 1.084 + \frac{0.0188}{\Theta} + \left(0.00161 + \frac{0.02661}{\Theta}\right) \lambda - \left(\frac{0.02833}{\Theta^2} - \frac{0.007828}{\Theta^3} + \frac{0.0007304}{\Theta^4}\right) \lambda \quad (2.7.9)$$

where $\Theta = 5040/T$ and in free-bound processes the Gaunt factor takes the form

$$g^{f-b} = a_n + b_n \lambda + c_n \lambda^2 \quad (2.7.10)$$

where a_n , b_n , c_n depends on the transition state with principal number n and λ is in microns.

appear in figure 2.4. The opacities were calculated as described Vernazza, Avrett, and Loeser (1976), thus, the absorption coefficient in units of cm^{-1} is given by

$$\alpha(\lambda) = \sum_{l=1}^8 n_l \left(1 - \frac{1}{b_l} e^{\frac{-h\nu}{k_B T}} \right) \sigma_l(\lambda) \times 10^{-18} \quad (2.7.11)$$

where $\sigma_l(\lambda)$ is the cross section. For our model the departure coefficient b_l becomes the unit because H, Si and C are treated in local thermodynamic equilibrium. The Hydrogen cross section is given by

$$\sigma_l(\lambda) = a_l \left(\frac{\lambda}{\lambda_l} \right)^3 g(\lambda), \quad a_l = 7.93 l \quad (2.7.12)$$

where a_l is the threshold photoionization cross section. Besides for Silicon $\sigma_l(\lambda)$ is

$$\sigma_l(\lambda) = \begin{cases} 0 & \lambda > \lambda_l, \quad 1 < l \leq 8 \\ a_l \left(\frac{\lambda}{\lambda_l} \right)^{s_l} & \lambda \leq \lambda_l, \quad 2 < l \leq 8 \end{cases} \quad (2.7.13)$$

and for the energy level $l = 1$ we used

$$\sigma_1(\lambda) = \begin{cases} a_1 & \lambda_1 \geq \lambda \geq 0.135 \mu\text{m}, \quad l = 1 \\ a_1 \left(\frac{\lambda}{0.135} \right)^{s_1} & \lambda \leq 0.135 \mu\text{m}, \quad l = 1 \end{cases} \quad (2.7.14)$$

where s_l is the spectral index. Finally, the Carbon cross section is obtained from

$$\sigma_l(\lambda) = a_l \left(\frac{\lambda}{\lambda_l} \right)^{s_l} - c_l \left(\frac{\lambda}{\lambda_l} \right)^{s'_l} \quad (2.7.15)$$

where

$$\begin{aligned} c_1 &= 28.2, & s'_1 &= 3, \\ c_2 &= 18.4, & s'_2 &= 2.5, \\ c_3 &= 24.0, & s'_3 &= 2.5, \end{aligned} \quad (2.7.16)$$

On the following table are the atomic data such as statistical weights, the threshold ionization wavelength, the photoionization cross section and the spectral index that we implemented to develop the H, Si and C calculations.

Atom	level <i>l</i>	Term	Statistical weight ϖ^*	Photoionization Wavelength Å	Photoionization cross section a_l	Spectral index s_l
Hydrogen	1	1s ² S	2	911.9	6.32	3
	2	2	8	3636	14	3
	3	3	18	8155	21.5	3
	4	4	32	14280	29	3
	5	5	50	22050	36.3	3
	6	6	72	31270	44.5	3
	7	7	98	44670	54.7	3
	8	8	128	58410	63.2	3
Silicon	1	3p ² ³ P	9	1525	37	5
	2	3p ² ¹ D	5	1682	35	3
	3	3p ² ¹ S	1	1986	47	0.5
	4	3p ² ⁵ S	5	3085	15	3
	5	4s ³ P ⁰	9	3864	1.25	2
	6	4s ¹ P ⁰	3	4040	4.09	2
	7	3d ³ D ⁰	15	4892	18	3
	8	4p ³ S,P,D	27	5840	14.1	3
Carbon	1	2p ² ³ P	9	1100	40.4	2
	2	2p ² ¹ D	5	1239	28.7	1.5
	3	2p ² ¹ S	1	1444	33.6	1.5
	4	2p ³ ⁵ S ⁰	5	1745	1	3
	5	3s ³ P ⁰	9	3257	0.2	1.2
	6	3s ¹ P ⁰	3	3437	1.5	1.2
	7	2p ³ ³ D	15	3733	16	3
	8	3p ³ S,P,D	27	4907	2.1	1.5

 $^*\varpi = 2J + 1$. J is the total angular momentum quantum number.

 Table 2.1: Atomic data of our H, Si and C eighth energy levels model from Vernazza, Avrett, and Loeser (1976, 1981); Wiese and Fuhr (2009); Kramida *et al.* (2013)

CHAPTER
THREE

OBSERVATIONS

This chapter presents the data work that we have developed to measure the white-light excess during solar flares. It introduces the HMI instrument that took the images (§ 3.1), the data set that was selected (§ 3.1.1) and the method established to obtain the white-light fluxes from each flare (§ 3.2) based on the advantages that show the HMI/continuum images for the study of WLFs such as spatial resolution, cadence and the 24-hour continuous observing sequence.

3.1 Solar Dynamics Observatory: Helioseismic and Magnetic Imager

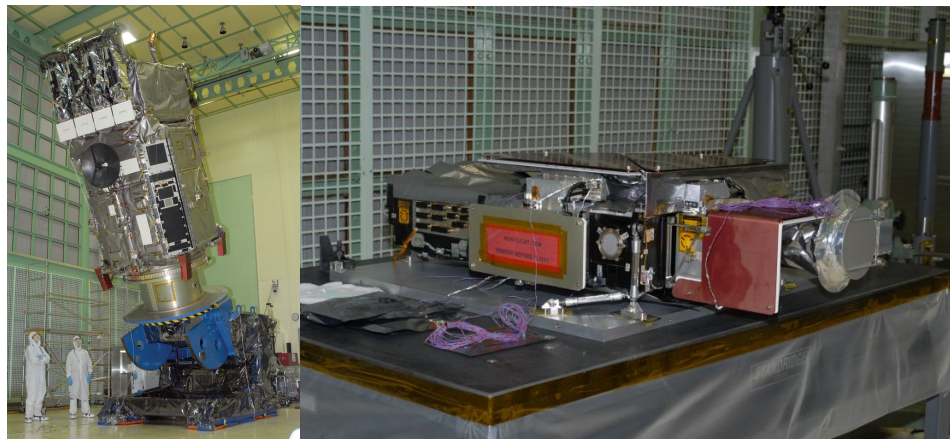


Figure 3.1: *Right* - Solar Dynamics Observatory (SDO). *Left* - Helioseismic and Magnetic Imager instrument on board the SDO.

Currently, the *Solar Dynamics Observatory* (SDO) is the biggest satellite observing the Sun and was launched on February 11, 2010 (see figure 3.1, left). It has three different instruments: The *Helioseismic and Magnetic Imager* (HMI), the *Atmospheric Imaging Assembly* (AIA),

and the *Extreme Ultraviolet Variability Experiment* (EVE). Either three instruments are very important to study the Sun and its phenomena; we limit our description of the HMI instrument and its images that were used in this work.

The Helioseismic and Magnetic Imager (see figure 3.1, right) was developed by the University of Stanford and its principal investigator is P. H. Scherrer. HMI was designed to study the solar oscillations and its magnetic fields above the photosphere. It is able to take full solar disk images at 6173 Å with a resolution of 1 arcsecond. HMI performs three kind of observations: Magnetic field (on the line-of-sight and vector magnetograms), velocities over the solar surface (Doppler imager), and the intensity of the continuum to observe features over the photosphere.

In order to detect the white-light excess during a solar flare, we have chosen the continuum images called HMI/Intensities as well. These images look at the Fe I absorption line with central wavelength at $6173.3 \text{ \AA} \pm 0.1 \text{ \AA}$. HMI/Intensities are the product of a reconstruction of the line-profile with 12 polarization images within Fe I line. Each sub-image has a filter bandwidth of $76 \text{ m\AA} \pm 10 \text{ m\AA}$ FWHM, and with a filter tuning range of $680 \text{ m\AA} \pm 68$. As a result of the reconstruction process, HMI/intensities have a cadence of 45 seconds.¹.

3.1.1 Data set

We analyzed 43 flares that occurred since October, 2010 to 31 July, 2012 with a GOES-classification greater than M1.0 and were observed by both satellites SDO/HMI and RHESSI.^{2,3} The locations of each event over Sun's surface are on figure 3.2.

Year	Initial number of flares		White light flares	
	M class	X class	M class	X class
2010	1	0	1	0
2011	21	4	11	4
2012	17	0	11	0
Total		43		27

Table 3.1: Set of flares analysed. In second and third columns are tabulated the flares with GOES-classification greater than M1.0 observed by SDO and RHESSI. In fourth and fifth columns are tabulated flares that presented a *clear* enhancement in white light observed by HMI/intensity.

¹For more information about HMI <http://hmi.stanford.edu/>

²Reuven Ramaty High Energy Solar Spectroscopic Imager (RHESSI)

³This set of flares was observed by both satellites, RHESSI and SDO. This constrain is because this group of flares was part of a previous work presented in the RHESSI Meeting 2012: Tracing the Connections, Petaluma, California - USA. And in the American Geophysical Union's 45th annual Fall Meeting, San Francisco, California - USA. See poster in appendix section.

We used a time range of one hour for all flares, thus for each event were downloaded 80 HMI/intensity images (2.7 GB in total per event). Moreover, the WL emission occurs in the impulsive phase (§ 1.2), so the time range chose was taking into account that the flare's peak observed in GOES channel 1-8 Å must be in the forty minute (see table 3.1). Additionally, to figure out which of those events present an excess in white light was performed the first data analysis developing the integration- and mean-differences methods (the explanation of these methods is found in subsequent sections). Therefore, we concluded that only 27 of the 43 events showed an enhancement in the HMI/intensity and they are considered as white-light flares.

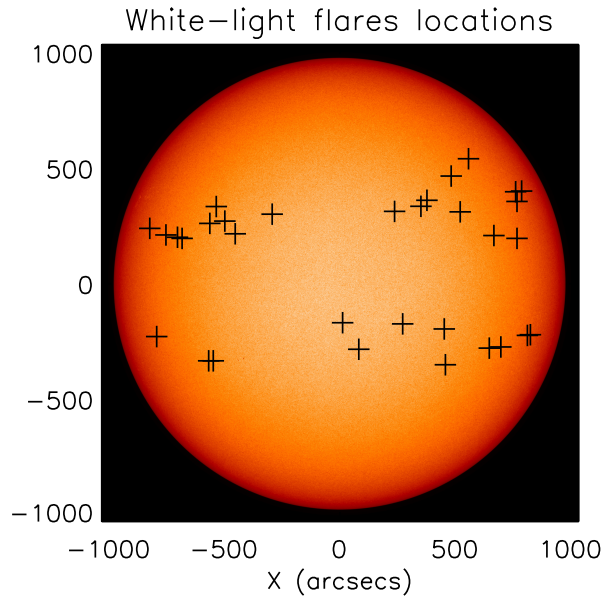


Figure 3.2: White-light flare sample. The checked points are their location over the solar disk.

3.2 Differences and mask methods

The procedures that we have implemented to determine the white-light excess of the WLF events (see 5th and 6th columns on table 3.1) are explained step-by-step, as follows

1. The HMI/Intensity images were co-aligned based on the roll-angle of the satellite when each frame was taken.
2. The active region was tracked using the SolarSoftWare (SSW) routine *diff_rot.pro*. This procedure computes the differential rotation of the Sun for each image based on a reference image. For this case, we have chosen the frame that was taken 10 minutes before the GOES peak.
3. We focused only in the active region that hosted the flare and coordinates were supplied by RHESSI.

4. The background from the umbra, penumbra and quiet-sun have been subtracted. For this purpose we have applied tree difference methods
 - (a) Normal-differences (see figure 3.3, 3.7).
 - (b) Mean-differences (see figure 3.4, 3.8)
 - (c) Integration-differences (see figure 3.5, 3.9).

The comparison between methods is described on next section

5. Resulting of the normal and the integration differences the intensity on pixels the signal is one part of real one from flare, thus, we implement a reconstruction algorithm on the differences images (see figure 3.6, 3.10).
6. After the reconstruction, the images have two kind of signal on the pixels. The first one, are those pixels which have a white-light signal and the second class are those pixels without any WLF-signal that have an intensity almost zero due to the difference procedure. However, the task to discriminate which pixels have an excess on the intensity of the continuum is crucial because we do not want to lose information of produce artefacts. So, we have applied two kind of masks to the reconstructed images: the intensity mask which eliminates the majority of noise pixel and the photometric mask which is geometrical mask to focus only on the WL emission kernels (see figure 3.14).
7. The WL excess from each flare is measured (see figures 4.6, 4.7 and table 4.2).

In order to keep the coherence of this text, we explain those masks after the discussion about differences methods and following are the Normal-differences, Mean-differences, Integration-differences and the reconstructed signal images for the time evolution the M9.3 solar flare SOL-2011-07-30T02:12.0 (see figures 3.3, 3.4, 3.5, 3.6) and the X2.1 solar flare

SOL-2011-09-06T22:20.0 (figures 3.7, 3.8, 3.9, 3.10)

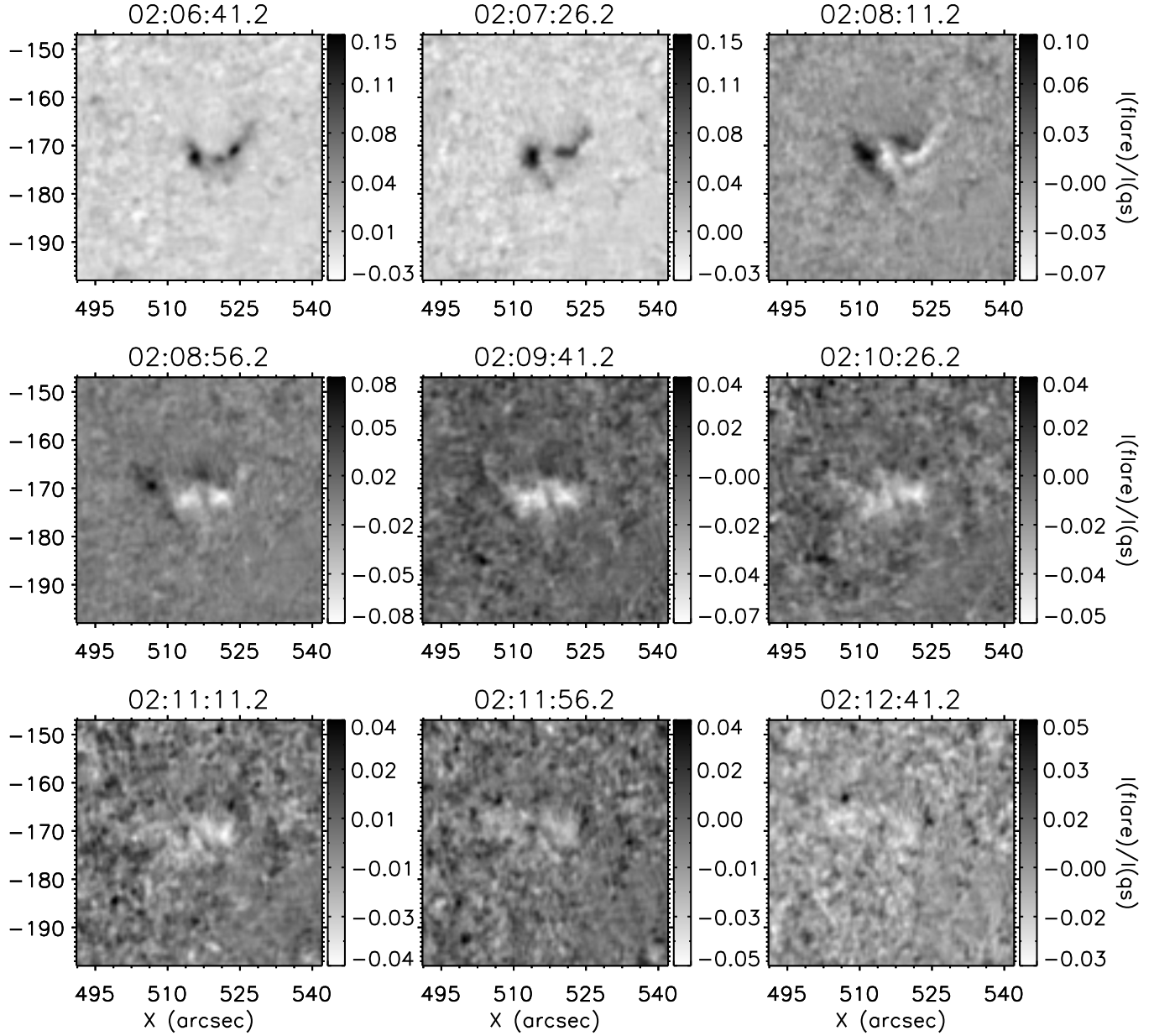


Figure 3.3: White-light flare SOL-2011-07-30T02:12.0 using the normal-differences method to subtract the background. The intensity has been normalized by the intensity of the quiet Sun at the center of the solar disk and the black-and-white color table has been reversed.

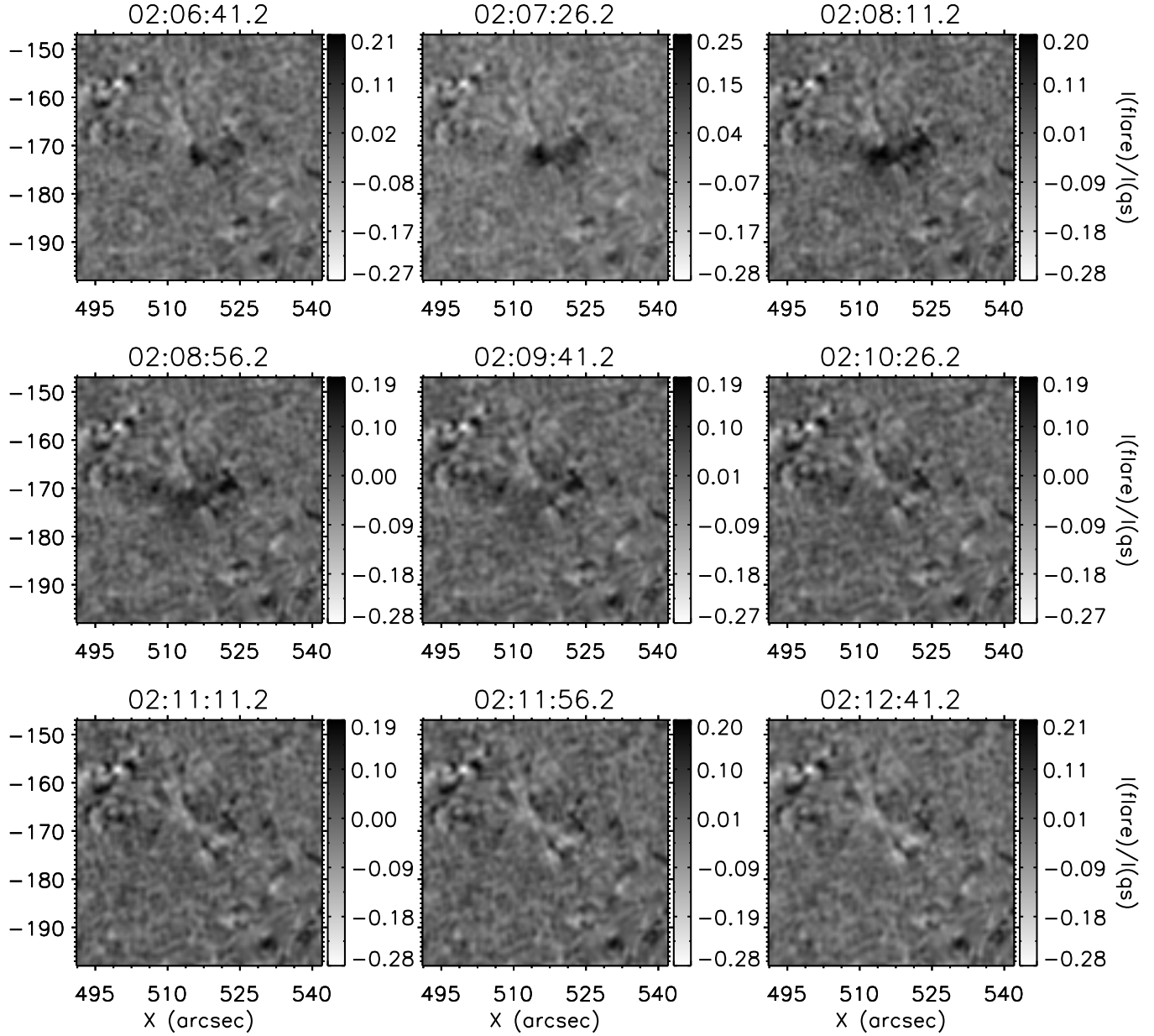


Figure 3.4: White-light flare SOL-2011-07-30T02:12.0 using the mean-differences method to subtract the background. The intensity has been normalized by the intensity of the quiet Sun at the center of the solar disk and the black-and-white color table has been reversed. We did not fix the scale in all images to present the intensities of the artefacts created by this method.

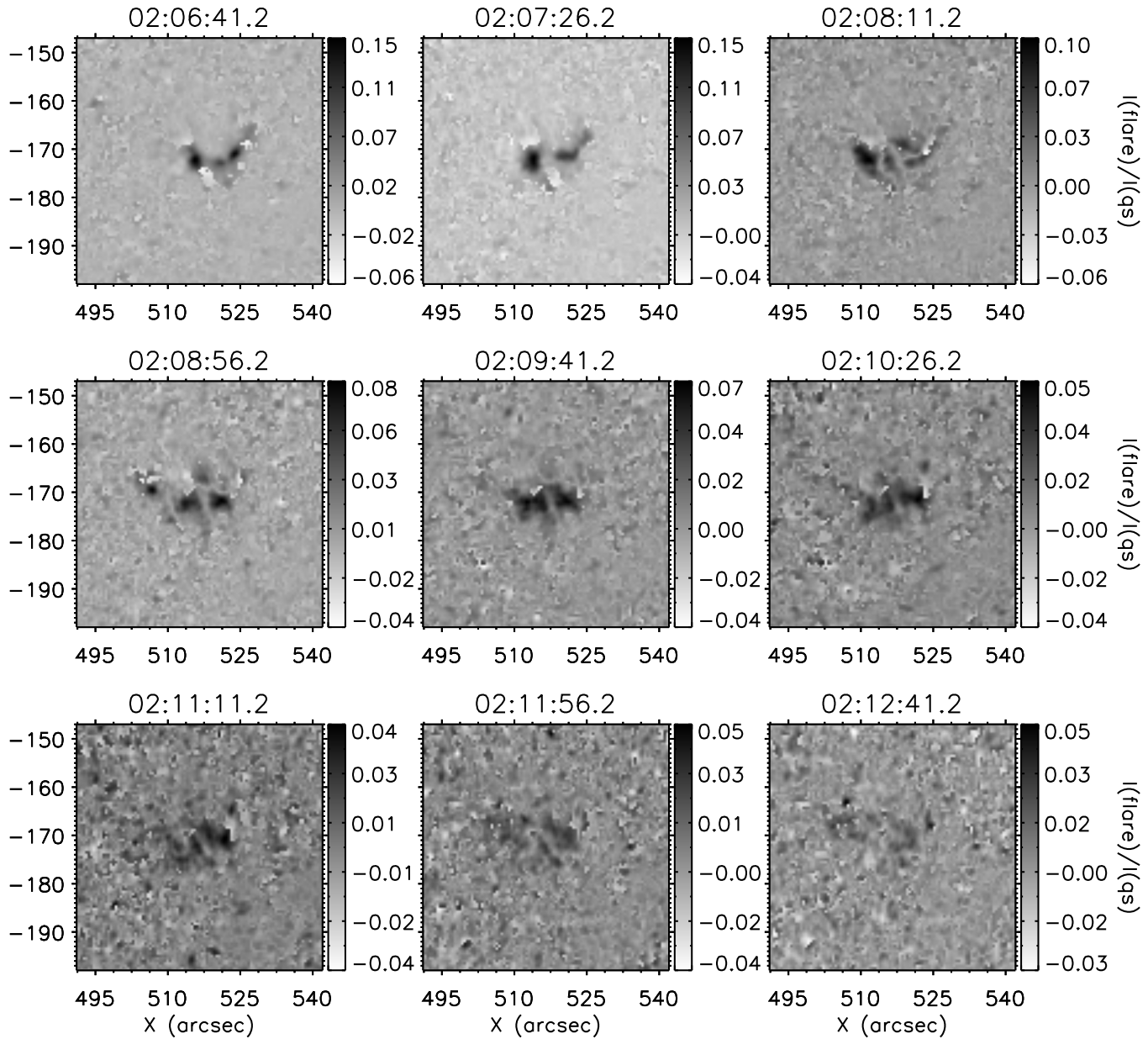


Figure 3.5: White-light flare SOL-2011-07-30T02:12.0 evolution using the integration-differences method to subtract the background. The intensity has been normalized by the intensity of the quiet Sun at the center of the solar disk and the black-and-white color table has been reversed.

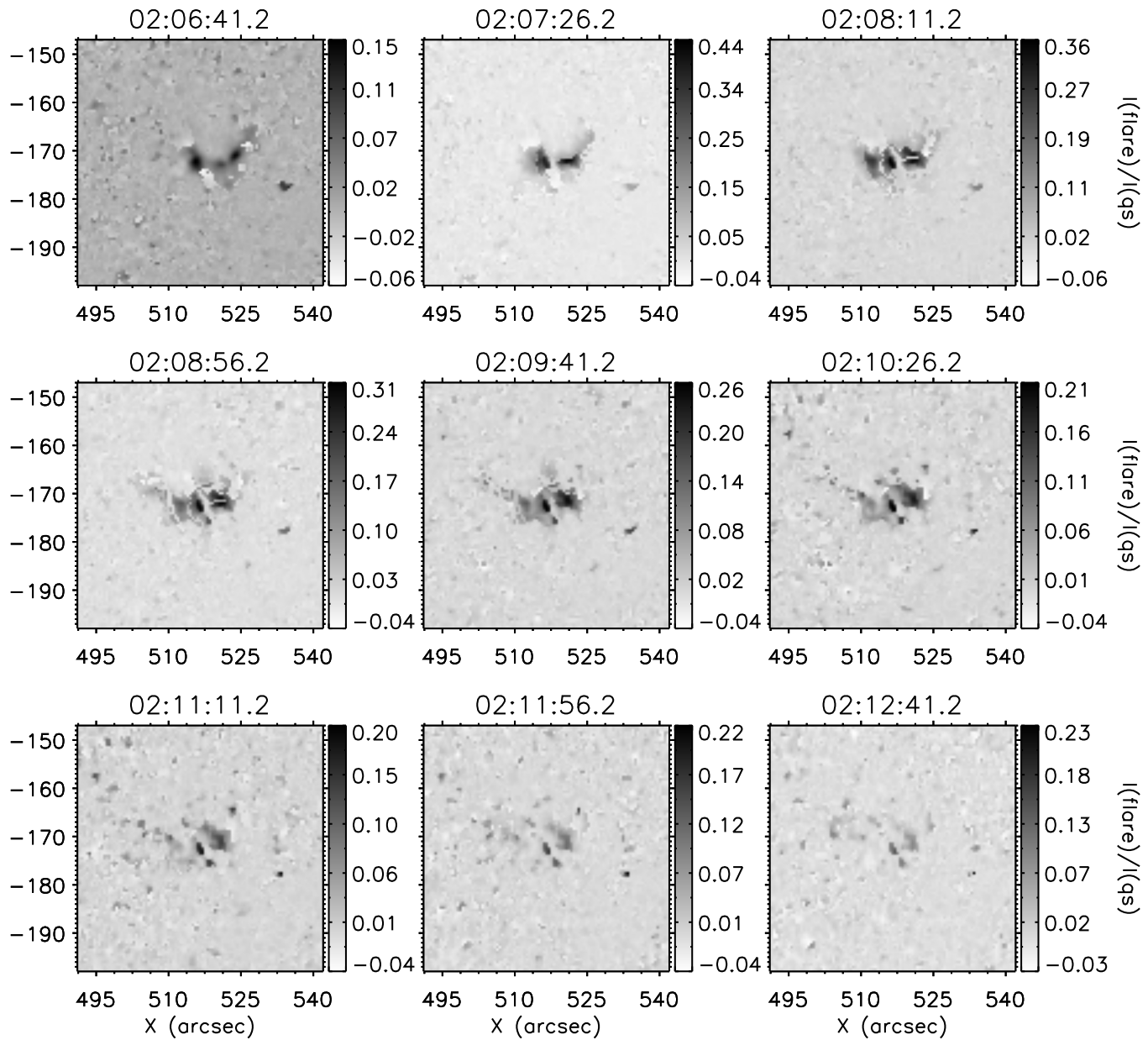


Figure 3.6: Reconstructed images of white-light flare SOL-2011-07-30T02:12.0 using the integration-differences method to subtract the background. The intensity has been normalized by the intensity of the quiet Sun at the center of the solar disk and the black-and-white color table has been reversed.

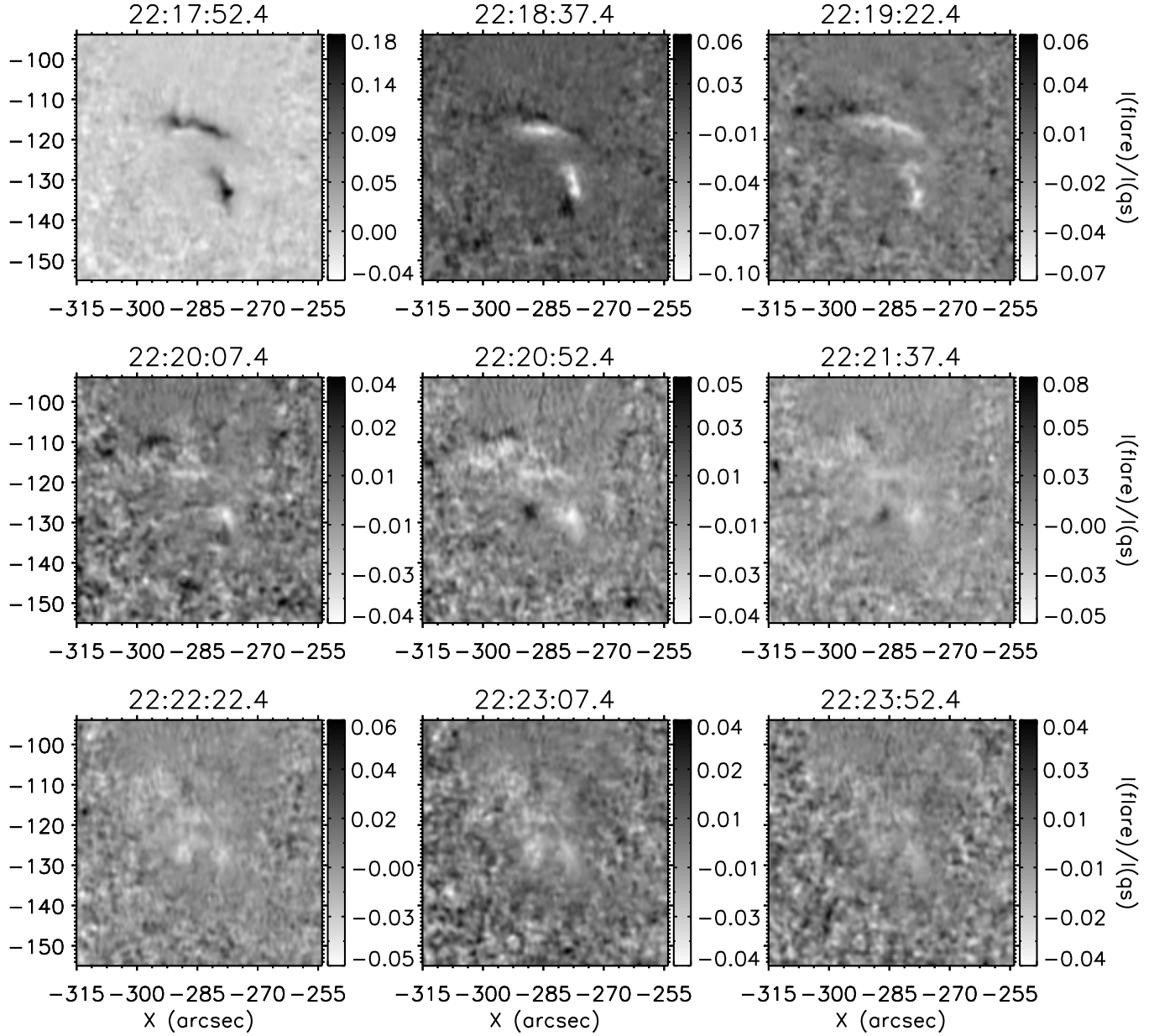


Figure 3.7: White-light flare SOL-2011-09-06T22:20.0 evolution using the normal-differences method to subtract the background. The intensity has been normalized by the intensity of the quiet Sun at the center of the solar disk and the black-and-white color table has been reversed.

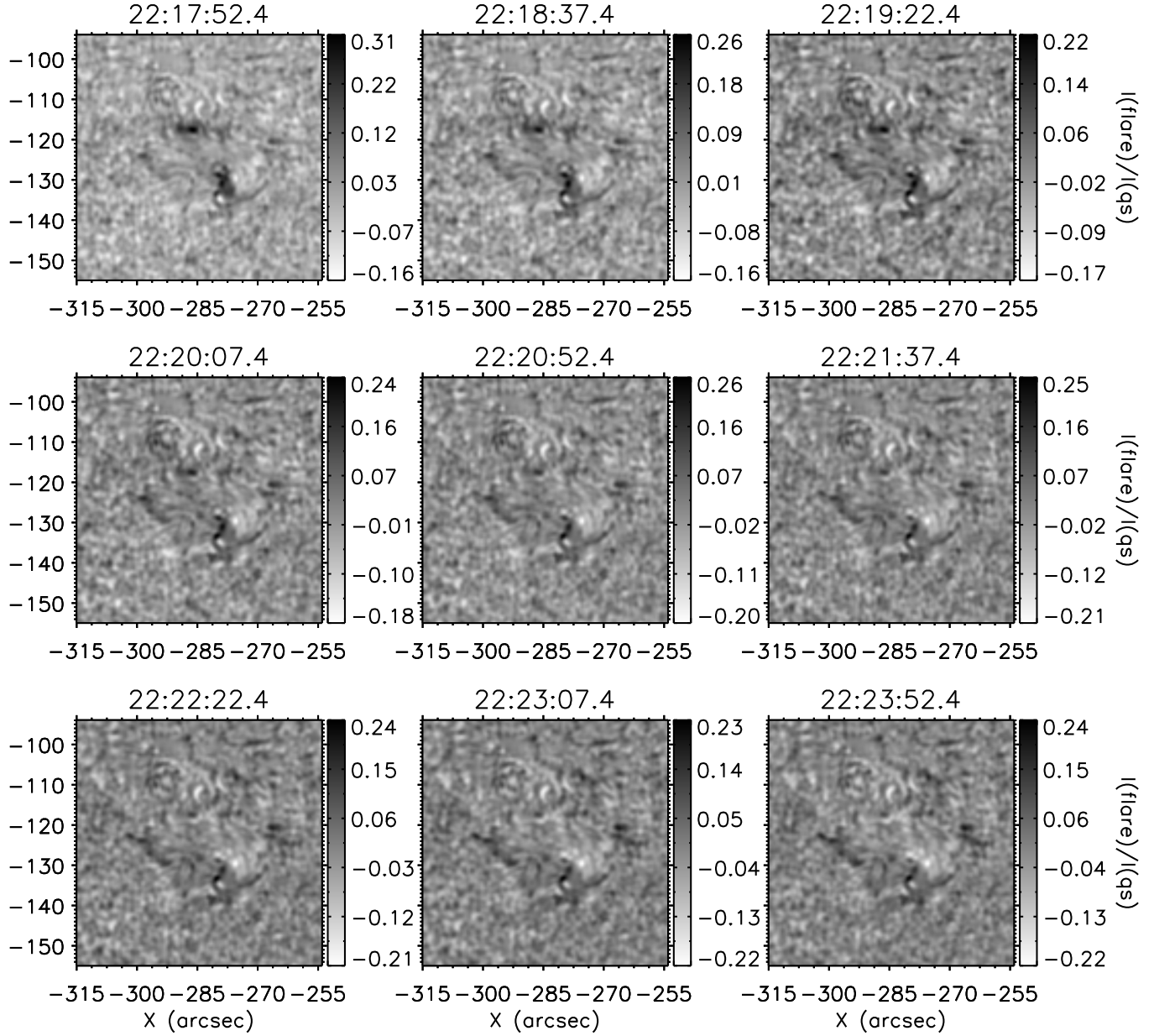


Figure 3.8: White-light flare SOL-2011-09-06T22:20.0 evolution using the mean-differences method to subtract the background. The intensity has been normalized by the intensity of the quiet Sun at the center of the solar disk and the black-and-white color table has been reversed. We did not fix the scale in all images to present the intensities of the artefacts created by this method.

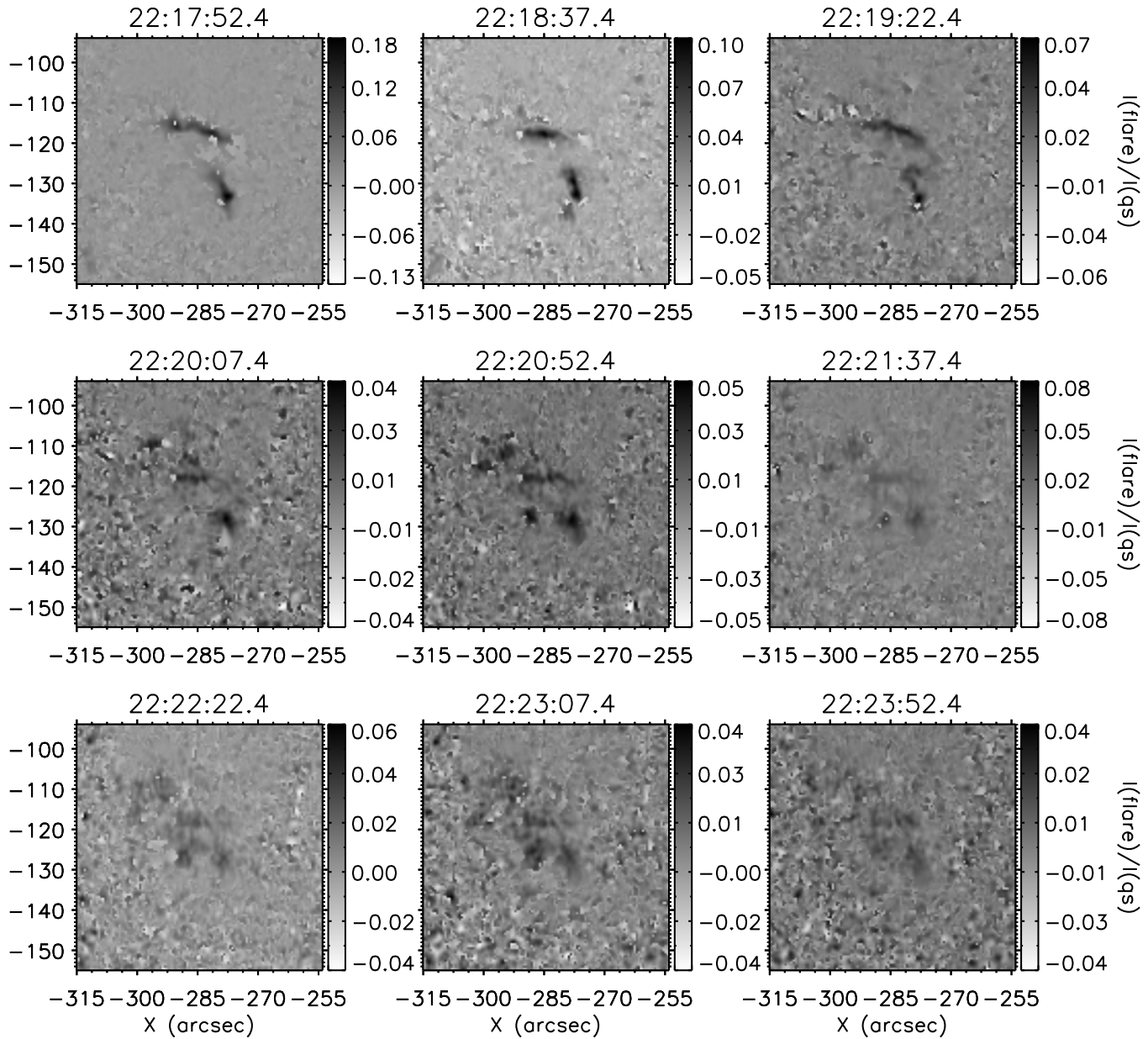


Figure 3.9: White-light flare SOL-2011-09-06T22:20.0 evolution using the integration-differences method to subtract the background. The intensity has been normalized by the intensity of the quiet Sun at the center of the solar disk and the black-and-white color table has been reversed.

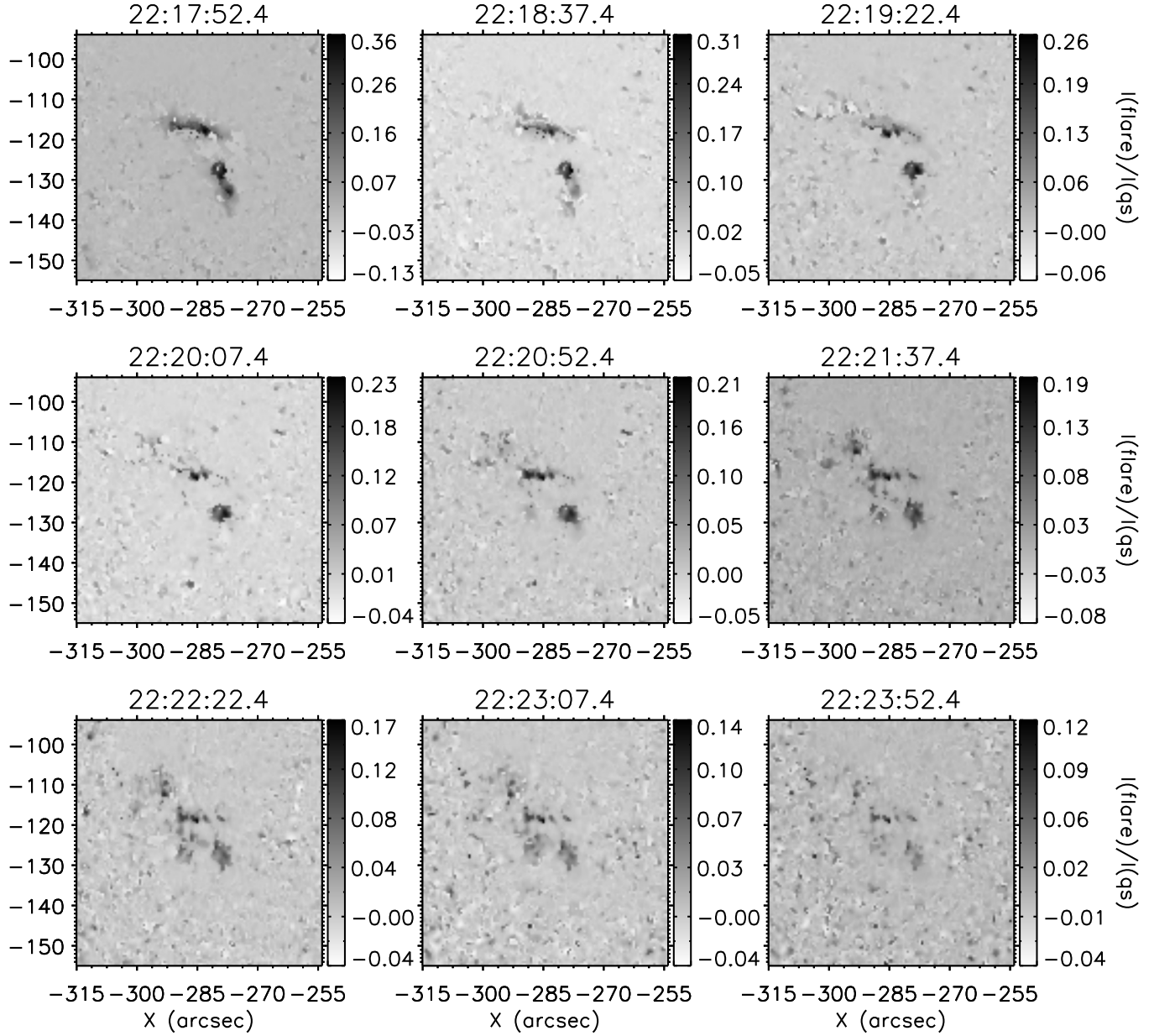


Figure 3.10: Reconstructed images of white-light flare SOL-2011-09-06T22:20.0 using the integration-differences method to subtract the background. The intensity has been normalized by the intensity of the quiet Sun at the center of the solar disk and the black-and-white color table has been reversed.

3.3 Differences methods

The normal- and mean-differences methods are usually used in solar physics (cf.(Hudson *et al.*, 1992; Matthews *et al.*, 2003; Martínez Oliveros *et al.*, 2011)). However, these methods provided two problems when one tries to obtain the white-light excess: ‘black’-WLF and non-physical artefacts. In the interest of solving this issue, we have proposed a new differences-method inspired on simple concepts: the extreme value theorem, the area under the curve and the integral identities.

3.3.1 Normal and mean-differences methods

The normal-differences method is implemented by taking a frame at i -time and subtracting the previous image. It performs as follows

$$I_i^{diff}(x, y) = I_{i+1}(x, y) - I_i(x, y), \quad i = 0, 1, \dots, N - 1 \quad (3.3.1)$$

where $I(x, y)$ is the intensity of the pixel with coordinates x and y . i represents the instrument’s cadence, which is $(i + 1) - (i) = 45$ seconds for SDO/HMI, and N is the total number of frames. See the time evolution of a flare using this method in figure ???. At performing this method the resulting images do not lose the cadence of the instrument. It means that the normal-differences method does not assume that the active region does not vary during one hour. This assumption is limited to study WLFs because flares, in most of the cases, are hosted over active regions¹. Thus, they are some pixels near the edge either umbra, penumbra or quiet-sun that may change from one zone of the active region to another one. Although, this method takes into account the instrument cadence and its resolution, it produces artefacts called ‘black’-WLF (see figure ??). This fake phenomenon is due to the difference after the maximum emission. The reason is that the frame at $(i - 1)$ -time have an greater intensity than the image at i -time, then, the resulting difference is less than zero (see figure 3.11, panel (B)).

The mean-differences method indicates that we have generated a mean image of the ten-first frames in the time range because we are sure that there is not any white-light signal in those frames. Subtracting the mean-image to every single frame we obtain the excess on white-light. In mathematical words

$$I_i^{diff}(x, y) = I_i(x, y) - I_{\langle 10 \rangle}^{mean}(x, y) \quad i = 0, 1, \dots, N \quad (3.3.2)$$

$$I_{\langle 10 \rangle}^{mean}(x, y) = \frac{\sum_{i=0}^{10} I_i(x, y)}{10} \quad (3.3.3)$$

¹The question if all flare are hosted in an active region is still open, and this work does not pretend to answer it.

Although, this method is a useful mechanism to remove the background signal from the data cube (see figure 3.11, panel (C)), it present some disadvantages. Firstly, this method imply that the active region will not change before and after a flare. This assumption is inapplicable for the high resolution data by SDO/HMI instrument. Secondly, employing this method we are losing information from the cadence of the instrument in those pixels on margin between umbra to penumbra or penumbra to quiet-sun, because those pixels in one time may be on one zone and in other time they may move to another one. Consequently, we create numerical artefacts on the resulting images applying this method.

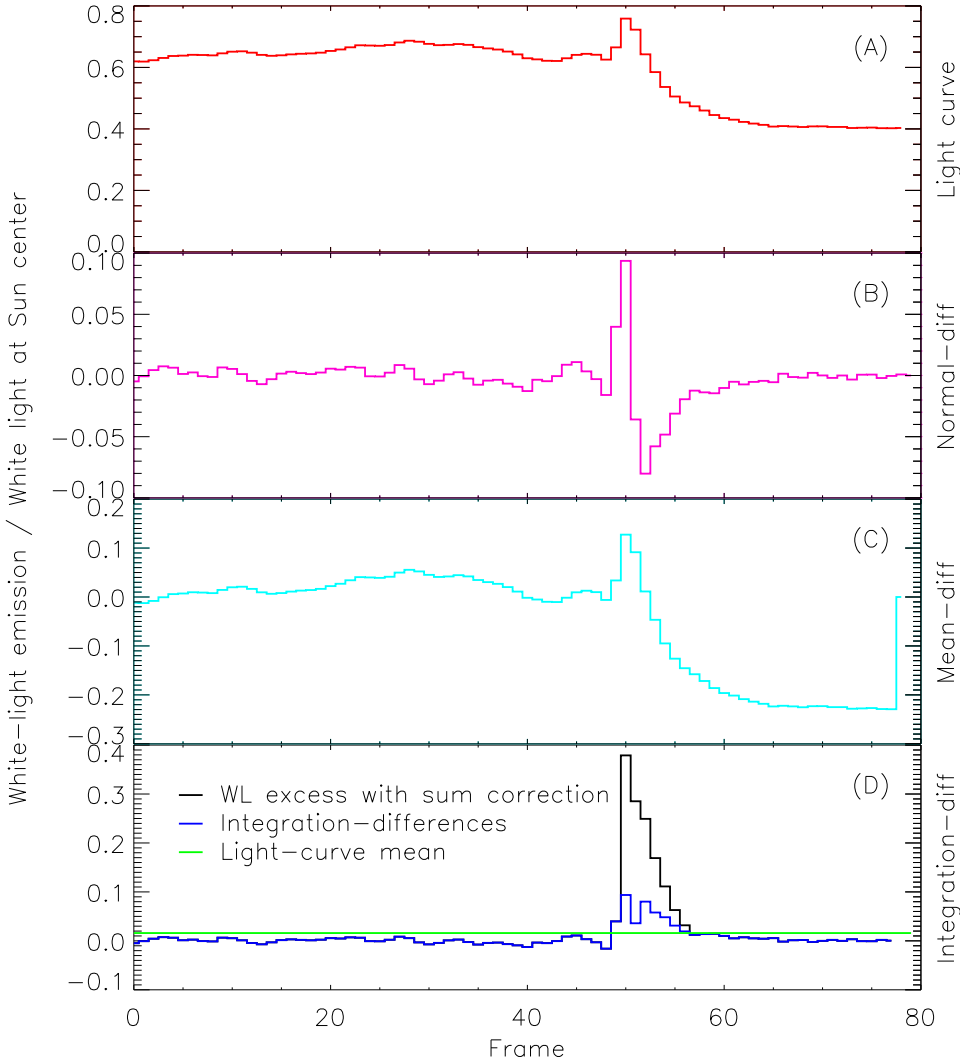


Figure 3.11: White-light curves of one pixel divided by the mean intensity at the center of the Sun. Panel (A) shows the light curve of a pixel. Panel (B) presents the light-curve of a pixel using the normal-difference method. Panel (C) presents the enhancement on the continuum intensity using the mean-difference method. Panel (D) shows the excess on white-light applying the integration-difference method. The time evolution has been plotted using the frame, i.e. the instrument cadence is the interval between one frame to another. In this case is 45 seconds.

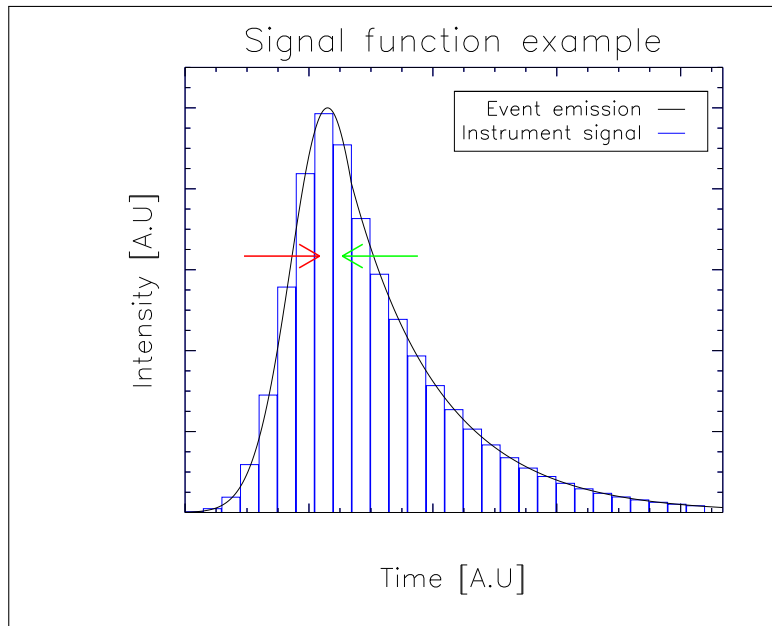
3.3.2 Integration-differences method

Now, we have proposed the integration-differences method to solve the disadvantages of the classic methods. This new method is bases on the definition of the excess that is the area under the curve subtracting the background. This concept is similar to the geometric definition of the integral, therefore, it let us to apply two results from the integral calculus (Thomas and Finney, 1996)

1. The extreme value theorem: If a real-valued function $f(t)$ is continuous in the closed and bounded interval $[a, b]$, then $f(t)$ must attain a maximum and a minimum, each at least once.
2. Additive property of integrals:

$$\int_a^c f(t)dt = \int_a^b f(t)dt + \int_b^c f(t)dt \quad (3.3.4)$$

Figure 3.12: Cartoon of a solar flare signal. The width of the blue bars means the cadence of the instrument. The red and green arrows show the direction to perform the differences on the integration method.



The first result suggests that in each pixel its light-curve has a maximum during the observation time. Moreover, if there is a WLF during the observation time the maximum of the light-curve will coincide with the maximum of WL emission. The second property let us to measure the area under the signal-curve in two subintervals before and after the maximum of the emission. Besides, we can breakdown the difference problem in two subintervals. We performed the normal-differences method for the interval before the maximum (i_{max}), i.e. we

subtract pixel-by-pixel to the image at time i the frame that was taken one time before ($i - 1$). In contrast, we invert the time-direction to perform the differences on subinterval after the signal peak, i.e. we subtract the intensity from the image at time i the image taken at time ($i + 1$). The arrows red and green on figure 3.12 represent the direction of the differences. In addition, this algorithm can be explained as

$$I_i^{diff}(x, y) = \begin{cases} I_{i+1}(x, y) - I_i(x, y) & \text{If } 0 \leq i \leq i_{max} \\ I_i(x, y) - I_{i+1}(x, y) & \text{If } i_{max} \leq i \leq N - 1 \end{cases} \quad (3.3.5)$$

Finally, if we just perform the differences, we would be measuring only the variation on signal between time i and time ($i + 1$) or in the opposite direction in the subinterval after the peak. In order to reconstruct the signal, we have added iteratively the difference-intensity of the previous or later frame, depending on the subinterval, to the value at that time. The flux diagram on figure 3.13 presents the reconstruction algorithm for the subinterval before the maximum. In addition, for the second subinterval the flux diagram is the same but inverting $i - 1$ by $i + 1$. As a result, on figure 3.11 - panel (D), there is an example of the differences-signal applying this method (blue line) and the reconstructed one (black line).

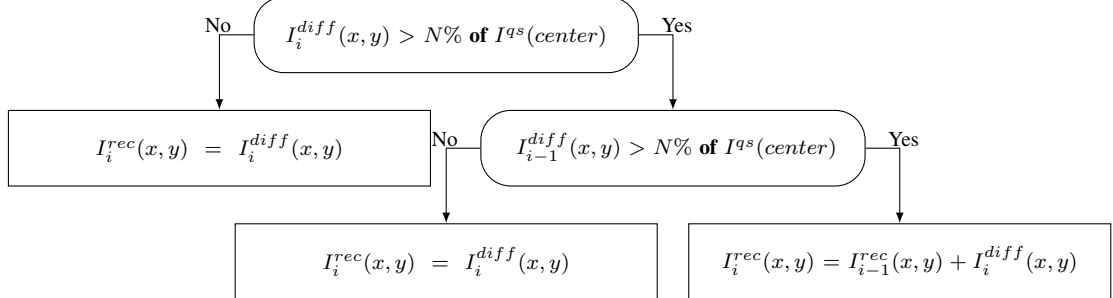


Figure 3.13: Flare's signal reconstruction algorithm for integration-difference method.

where I_i^{rec} is the signal reconstructed, N is the percentage of the quiet-sun-intensity-average measured at the center of solar disk $I^{qs}(center)$. We have tried different values for N , however, we concluded that N must vary between $0.5 < N \leq 5$ because for values greater than 5% we might be losing information from those pixels with weak WL intensities. To sum up, we have solved the ‘black’-WLF problem doing a time-reverse on the differences. Moreover, we have improved the assumption of the mean-differences method about a non-strong evolution of the active region during a flare proposing a new differences method, which implies that the evolution of the active region measurable just depends on the instrument cadence but not on the numerical analysis.

3.3.3 Masks

After the implementation of the differences on the data cube, we want to measure the white-light flux in each image. However, on the difference-image there are not only pixels with white-light emission, but also noise pixels outside of the emission kernels. To distinguish between both classes of pixels, we apply the N -mean mask and photometric mask to the difference-images.

- (i) *Intensity mask* takes advantage that value in the most of noise pixels is close to zero after the differences. Therefore, for those pixels with an intensity less than N ($0 < N \leq 5.0$) percent of the quiet-sun intensity will become zero (see left panel in figure 3.14, and compare with figures 3.5 and 3.9). Although, after performing the intensity mask over the data, there is still some noise pixels because we do not want to impose a strong condition ($N > 5.0$), which may carry losing information of some pixels with a weak white-light enhancement (read discussion in § 4.2). Consequently, we need to figure out another kind of mask to eliminate the remaining noise pixels.
- (ii) *Photometric mask* will eliminate leftover noise pixels applying a geometry mask. This mask consists in a circle with changeable radius and center coordinates. Radius depends of the kernel size for each flare, and its position adapts to the location of maximum intensity pixel (see figure 3.14, right). Therefore, those pixels outside the circle will become zero on their intensities.

Finally, the enhancement in white-light during a flare is computed for each image. The observational results are shown on next chapter.

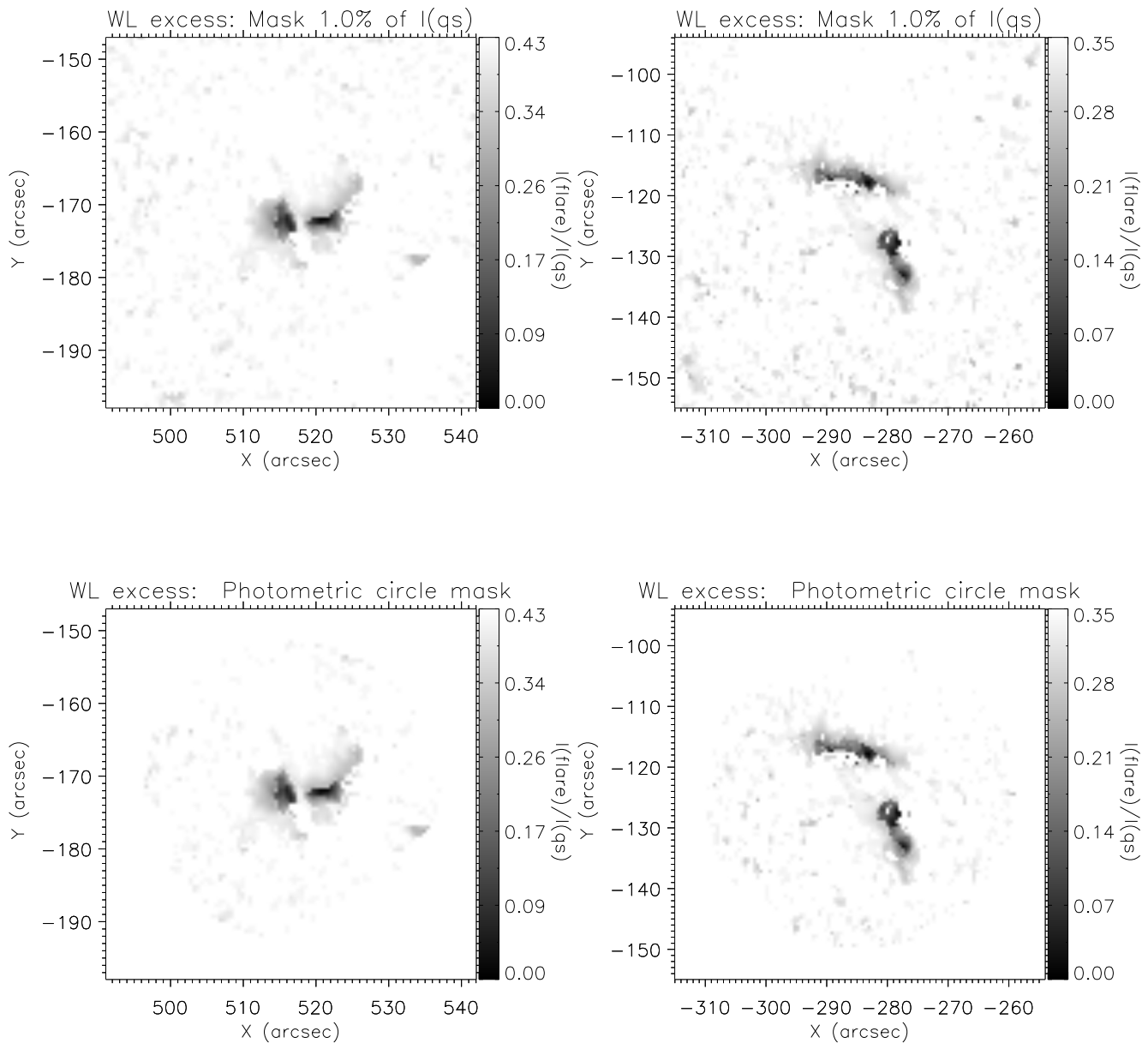


Figure 3.14: Example of the intensity mask (*top*) and photometric mask (*bottom*) applied on a reconstructed images of flares SOL-2011-07-30T02:12.0 (*left*) and SOL-2011-09-06T22:20.0 (*right*).

CHAPTER FOUR

DISCUSSION

Along this work it has been presented the concepts of the observational and numerical approaches that we implemented to analyse the white-light enhancement during solar flares and in this chapter we are going to discuss the results achieved.

4.1 Atmospheric model results

The Backwarming model (Machado, Emslie, and Avrett, 1989) postulates that the emission on the intensity of continuum is due to recombinations of the negative hydrogen ion H^- which is the main source of opacity in the stellar-atmospheres such as the Sun or by hydrogen free-bound emission in the upper chromosphere. Furthermore, the emission of the H or H^- has a strong correlation with the medium temperatures which increase as same as the region is heated, then, the white-light may be produced by this mechanism with a requirement of a physical process to achieve temperatures about 10^4 K on upper chromosphere or 100K around the temperature minimum. The mechanism proposed to achieve these temperatures are the

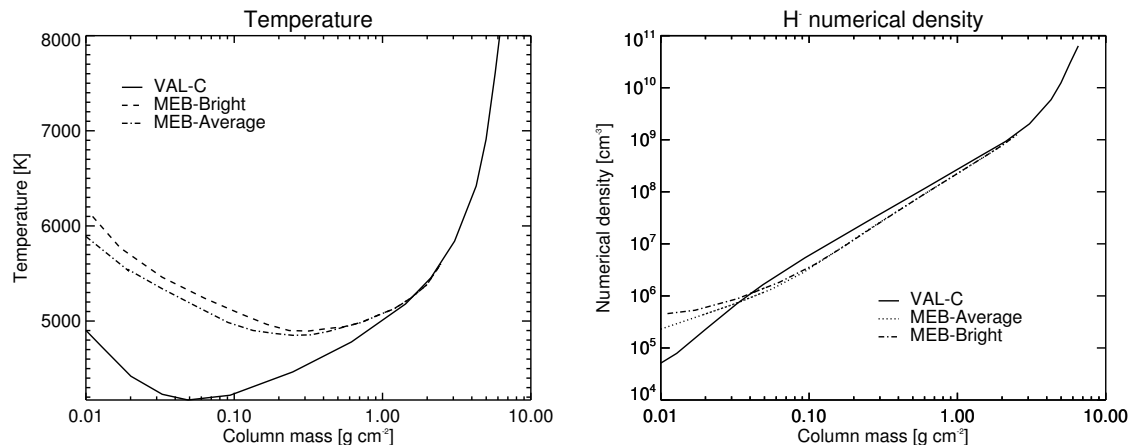


Figure 4.1: Temperatures and H^- density profiles throughout solar atmosphere where hight densities mean lower slabs.

XUV radiation field. Thus, to contrast this model we carried out LTE calculations for H, H⁻, Si and C with flare-atmospheric conditions proposed by Machado, Emslie, and Brown (1978).

To have an idea what are the qualities of flare-atmospheric conditions we have over-plotted the empirical quiet-sun atmospheric model developed by Vernazza, Avrett, and Loeser (1973, 1976, 1981). On figure 4.1-left are temperatures profiles of VAL-C and MEB where the main difference between them is the height, over photosphere, of the minimum of the temperature which is ~ 500 km on VAL-C model and almost ~ 260 km on MEB model. In addition, we have treated the negative hydrogen ion in LTE conditions which in this case means that the departure coefficient equals one along the atmosphere. The comparison between quiet-sun and flare H⁻ numerical densities are on figure 4.1-right.

In our atmospheric model we have calculated the bound-bound transitions for H, Si and C with eight energy levels. The line-absorption coefficient due to these atoms is in figure 4.2-top. The edge shape means the threshold energy required to ionize the atom when the electron is in a n-energy state. Besides the middle and bottom panels show the H⁻ free-bound and free-free opacities calculated for atmospheres with and without flare perturbations.

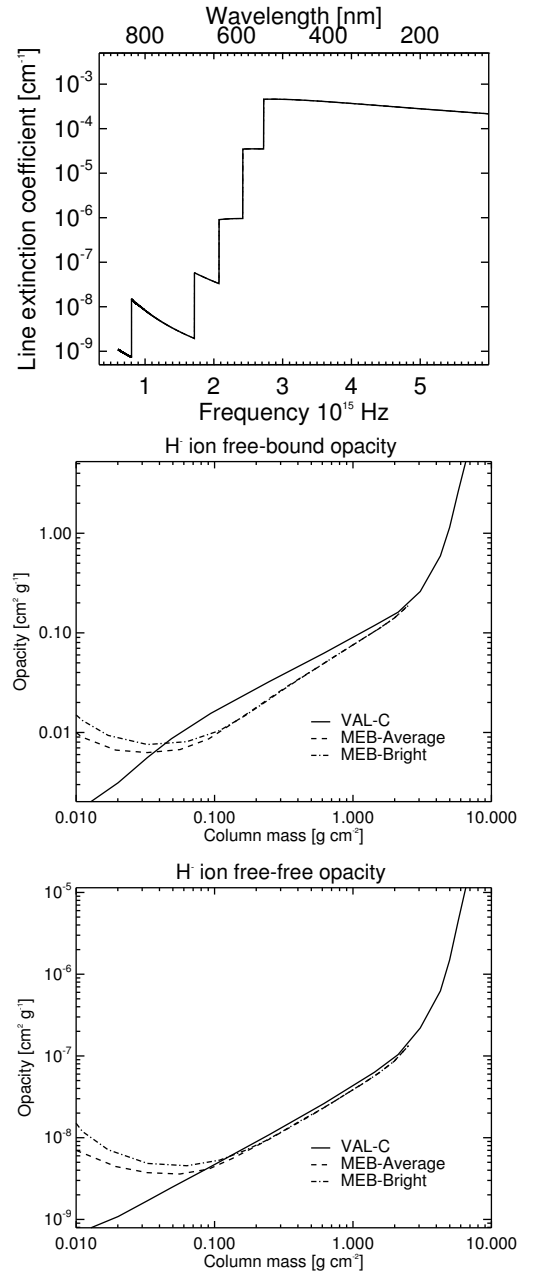


Figure 4.2: The H, Si and C line-opacities (top). H⁻ free-bound and free-free opacities (lower panels, respectively).

To observed if the XUV mechanism is able to achieve suffice heat on lowers layers of atmosphere we have calculate the net radiated cooling function Ψ in units of $\text{erg cm}^{-3} \text{s}^{-1}$ as was presented on equation (2.5.4). This function describes if the source function S_ν is greater than the mean intensity J_ν in the region or on the other way around. On figure 4.3 is presented our calculations for bright and average flare conditions which were performed from the begin of the photosphere until $\sim 600\text{km}$ over it, i.e. after the temperature minimum for both flare models.

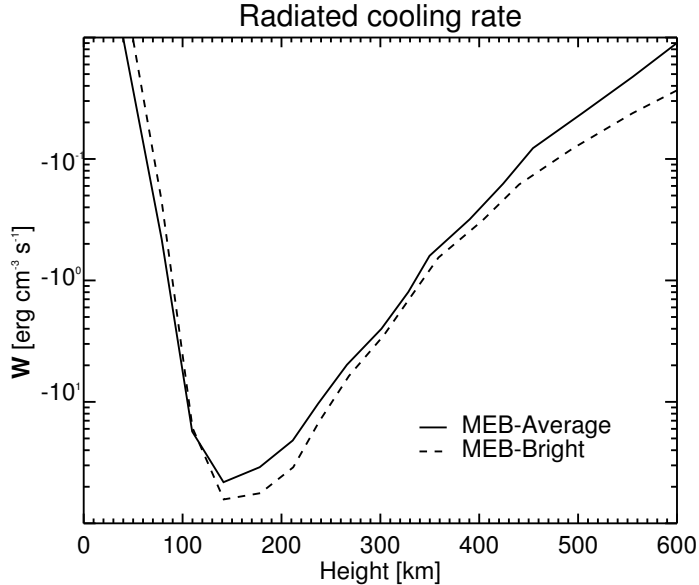


Figure 4.3: Net radiated cooling rate for flare conditions.

In this results we see a net heating (negatives values) from deep photosphere layers to regions after temperature minimum indicating that the XUV-backwarming process can account higher temperatures on lower regions of solar atmosphere to achieved the white-light emission by Hydrogen free-bound and the H^- recombination processes.

4.2 Observational results

Not only the white-light-flare problem is theoretical but also it represents and observational challenges in different ways. In this work we have been developing the first stage of the analysis, i.e., we attempted in different ways how to measure the white-light excess during flares. This is because we think this simple but not mentioned problem on solar literature may implicate over or sub- estimations of this physical quantity.

To analysed this problem we have considered 43 flares occurred on current solar maximum. We found that the 63% of flares presented a *clear* excess in white-light (see table

4.1). In figure 4.4 is presented the peak's frame of the M9.3 and X2.1 solar flares examples treated on chapter 3. The black arrows are directed to the WL emission kernels. Notice that the emission may take place either over umbra, penumbra or quiet-sun regions closer to the active region. Their location depends on a more general image of full-solar-flare process and its interactions with the magnetic configurations through each solar layer. In this way, one cannot assume where they may happen and they may not perturb the configuration of the active region, as a matter of fact, one can observe strong differences before, during and after the flare without any image process. As a consequence the classic method (in our notation the mean-differences method) developed by different authors e.g. Potts *et al.* (2010); Metcalf *et al.* (2003); Jess *et al.* (2008) presented some difficulties but also advantages.

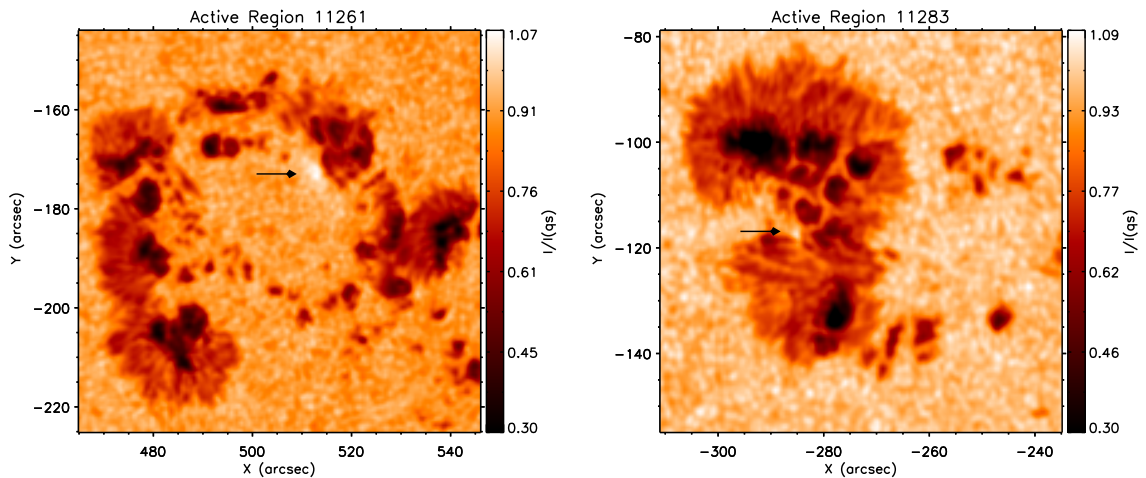


Figure 4.4: White-light emission at flare's peak observed by SDO/HMI. *Left* - The M9.3 GOES-class SOL-2011-07-30T02:12.0 flare. *Right* - The X2.1 GOES-class SOL-2011-09-06T22:20.0 flare. Black arrows show the WL emission kernels.

As was explained on chapter 3 the main-differences consist on subtract to the whole data either one reference image took before the flare or one mean-image from several non-flare images. This method carries the advantage that net signal after differences do not need any kind of reconstruction, however, it generates observable artefacts by the own evolution of the active region and those produced by the flare perturbations. This method also presents a strong correlation with the mask-threshold (see figures 3.4, 3.8). In addition, the normal-differences ($i - (i-1)$) presented 'black'-white-light artefacts due to subtract the flare's peak frame to the subsequent.

To solve these issues we propose a simple method called integration-differences to perform the differences which takes the advantage of the normal-differences, i.e. it subtracts one-by-one the subsequent or previous image depending on the subinterval (for complete

details on § 3.3.2). Nevertheless, this approximation requites a reconstruction step in contrast to classic method. This point is crucial because we do not want to add artefacts reconstructing the signal. Thus, we implemented as simple as possible a reconstruction algorithm to solve this issue and its description is on the flux diagram 3.13. Likewise, with this method there are a few pixels with very low flare intensities that have been lost due to the time reversal.

Even if it is chosen the mean, normal or integration differences method to achieve the flux measurements, it is necessary to eliminate those pixels with non-WL signal. The common method is apply a mask to the datacube. For our analysis we have used two kind of mask: a geometrical mask which surrounds the emission kernels with a circle, and a intensity-mask which eliminates pixels with an intensity less than a certain threshold intensity. However, choosing the threshold intensity is a rather important decision because one does not want to lose any flare's information. In this way, one alternative is choosing a percentage of the flare maximum intensity, notwithstanding, for flares with a strong emission the mask will not count weak pixels with WL-signal and for powerless WLFs this threshold will carry summing non-flare pixels. To figure out the threshold intensity we have adopted a percentage of a quantity that came from directly of the observations but it does not have a visible correlation with flares processes such the quiet-sun intensity at disk center.

At this point the following important remark must be made before we finish the debated of data analysis during WLFs. We have discussed in detail the differences, reconstruction and mask issues because we want produce a 'standard' reduction process of the continuum images as a result of the set of flares chosen is quite large, flares have different locations, GOES-classification and we do want to reduce as much as possible a partial view for each event.

To contracts between methods we have measured the WL intensity applying same masks in two differences method. One was the mean-differences as were performed by Metcalf *et al.* (2003), i.e. we subtracted to whole datacube the image that was taken before the flare's beginning and the integration method explained above. Thus, figures 4.6 and 4.7 show the WL-curve normalized by the intensity at center disk for both methods (black line). They also present the WL emission area (blue line) at each frame. Notice that we have left the time axis in number of frames because all flares were observed with the same time range and as a result the time in our reduction method is just a parameter. Each panel has a particular mask threshold intensity where it varies from 0.001% (left-bottom) to 5% (right-top) of the intensity at disk center.

Figure 4.6 shows a strong correlation between reference image and the intensity at each time. Notice that its minimum coincides with the reference frame but it is not zero because we changed the reference frame, just at this time, to the image took one time before. This behaviour is a consequence as the farther is the frame from the its differences reference, the more artefacts are created due to evolution of the active region as explained above. Furthermore, noise signal 15 minutes before and after achieved an intensity similar to the flare's emission which is an evidence that artefact in this method present an overestimation of the WL emission.

On the other hand, figure 4.7 shows that WL-curve measured applying the integration differences and its reconstruction. One can observed a dependency in how drastic is the mask but its shape is quite constant. Nonetheless, if we subtract the mean background from frame tenth to fortieth the intensity do not depend on the mask.

To measure the net intensity from both methods we chose the threshold intensity as 1.0% of quiet-sun intensity at disk center and we enclosed the time range to the duration of WL emission from flare. In case of the integration method we have subtracted the background as explained above. Moreover, to perform a quantitative analysis of the measurements it is needed a transform of HMI/continuum units from $DN\ s^{-1}$ to physical units. Conversion factor α was calculated using the daily mean solar irradiance data from the Total Irradiance Monitor (TIM) on board the SOlar Radiation and Climate Experiment (SORCE), and comparing with the total emission from non-flare HMI/continuum images accordingly to

$$I_{SDO} = \alpha I_{TIM} \quad \therefore \quad \alpha = \frac{I_{SDO}}{I_{TIM}} \quad (4.2.1)$$

Thus, net flare intensity in units of $Wm^{-2}sr^{-1}\text{\AA}^{-1}$ is given by $I_{flare} = \alpha^{-1} \sum_{i=t_0}^{t_f} I_i$; where i represents the i -frame, t_0 and $t_f = 45\ sec \times N$ are the WLF start and end times respectively, and N is the number of frames where flare emitted. Table 4.1 presents flares description such as data, start, end and peak time, their GOES classification, the WL emitting time and the conversion factor to physical units. In table 4.2 are the total WL intensity measured at 6173 Å and the total emitting area A in unit of $(Mm)^2$ using the mean and integration method. We also lists the total energy emitted at 6173 Å over a unit solid angle, per unit area A cross, per unit time Δt and with a passband $\Delta\lambda$ in units of joules (Kerr and Fletcher, 2014)

$$E_{\lambda}^{total} = \pi I_{\lambda}^{total} A \Delta\lambda \Delta t \quad (4.2.2)$$

where it has assumed isotropic radiation and $\Delta t = t_f - t_0$ is the total emission time and $\lambda = 6173\text{\AA}$. Table 4.1 presents the final results of our observation where is shown

that intensity, area and total energy emitted are much higher applying the Mean method. Authors think these discrepancies of one order of magnitude, in the majority of cases, may have two reasons: *i*) mean method produce non-flare artefacts which sum (in this method) to the total flare emission and the area measured. *(ii)* the masks performed over data may not be enough to find pixels with WL emission. A good candidate to create the masks (but no the differences) may be the method explained by Kerr and Fletcher (2014) which have achieved a very interesting results from the difficult event to measure: flare SOL2011-02-15T01:56:00. Nevertheless, even if mask were not enough strong to eliminate the non-flare pixels, the intensities of these pixels after differences procedure would not be significant comparing with flares intensity if the differences step would not present artefacts. As a result, we claim that classic methods of the first step in the WLF analysis must be considered in detail to achieve better results analysing these kind of solar process.

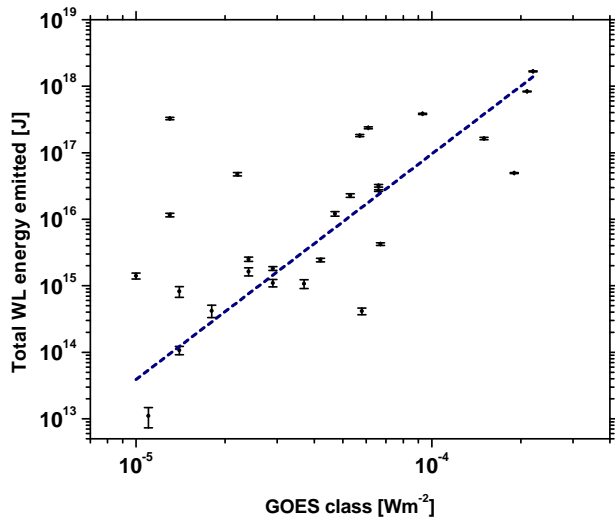


Figure 4.5: GOES-class (W m^{-2}) versus total WL energy emitted at 6173 \AA using the integration method

To conclude this work, on figure 4.5 is plotted the GOES-class (in units of W m^{-2}) versus the total WL energy emitted (in Joules) at 6173 \AA . This graphic may let us to observed if there is ‘Big Flare Syndrome’, i.e. the white-light emission only occur just on big flares. However, for different authors (e.g. Kerr and Fletcher (2014); Jess *et al.* (2008)) this radiative process is not unusual on flares and there is not yet a big picture of the enhancement in WL. Thus, in figure 4.5 it is observe a tendency between how energetic is the flare and now much energy was emitted on white-light. If we interpolate this graphic to low GOES classes, we primarily conclude that small flares will also emit in WL, and then, the syndrome would mean that it is necessary to understand better the low-energy regimes in terms of radiative transport mechanisms and with better instrumental and data reduction techniques.

4.3 Summary

We have developed a LTE radiative transfer code to model the heating on lower layers of solar atmosphere due to the XUV radiation proposed by (Machado, Emslie, and Avrett, 1989) around the temperature minimum for average and bright-flare conditions (Machado, Emslie, and Brown, 1978), which shown that backwarming process by XUV radiation field is able to heat lower atmosphere layers. However, our calculations are one order of magnitude lower than those performed by Machado, Emslie, and Avrett (1989). One reason to obtain this results may be that in our simple atmospheric model we only took into account the opacities for H, Si and C but we did not perform the radiated rates for this line-processes and other important elements such Ca and Mg. Also, it may occur because our treatment of H^- is in LTE resulting in a misinterpretation of the H^- processes.

We have implemented a new method to achieve the measurements of the white-light excess during flares. This method have been tested with the classic method such as the mean-and normal-differences concluding that the new method eliminates the majority of artefacts due to classical methods. Besides, we claim that classic and our method need to continue to be developed.

Finnaly, in a first stage of analysis we found that in our WLFs set there is a tendency between the total WL energy emitted and GOES class which is a parameter of how energetic was the flare. This tendency may account that small flares are able to produce WL enhancements as have presented by different authors such Hudson, Wolfson, and Metcalf (2006); Jess *et al.* (2008), however, we are aware to asseverate this conclusion because our data set did not account flare with GOES-classes less than M1.0 and the narrowband nature of the HMI/continuum observations.

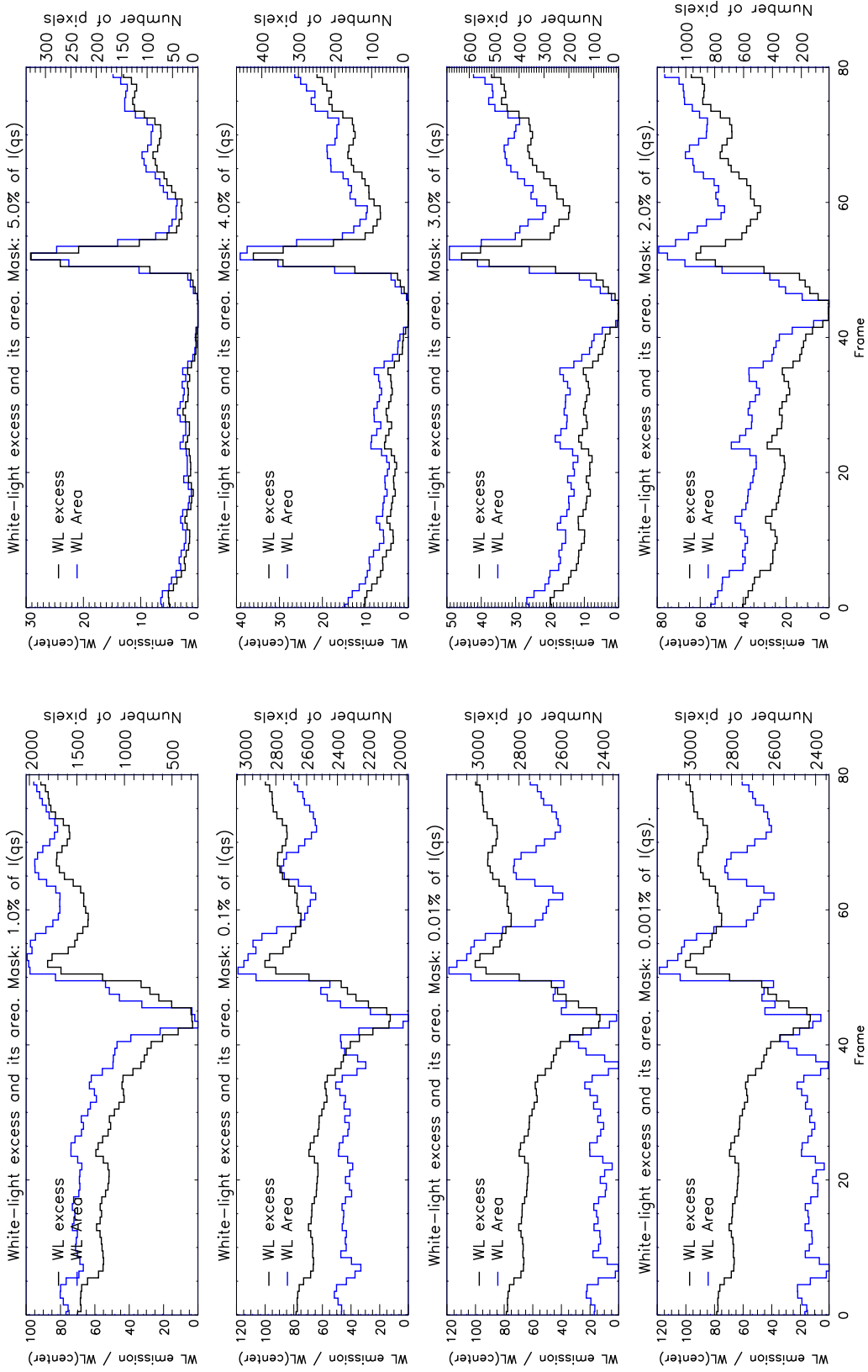


Figure 4.6: WL enhancement curve (blue line) and its area (black line) during flare SOL-2011-07-30T02:12.0. Flux was measured using the mean-differences, intensity and photometric masks. Each panel has a different value as zero level of mask which goes from 0.001 to 5.0 percentage of quiet-sun intensity.

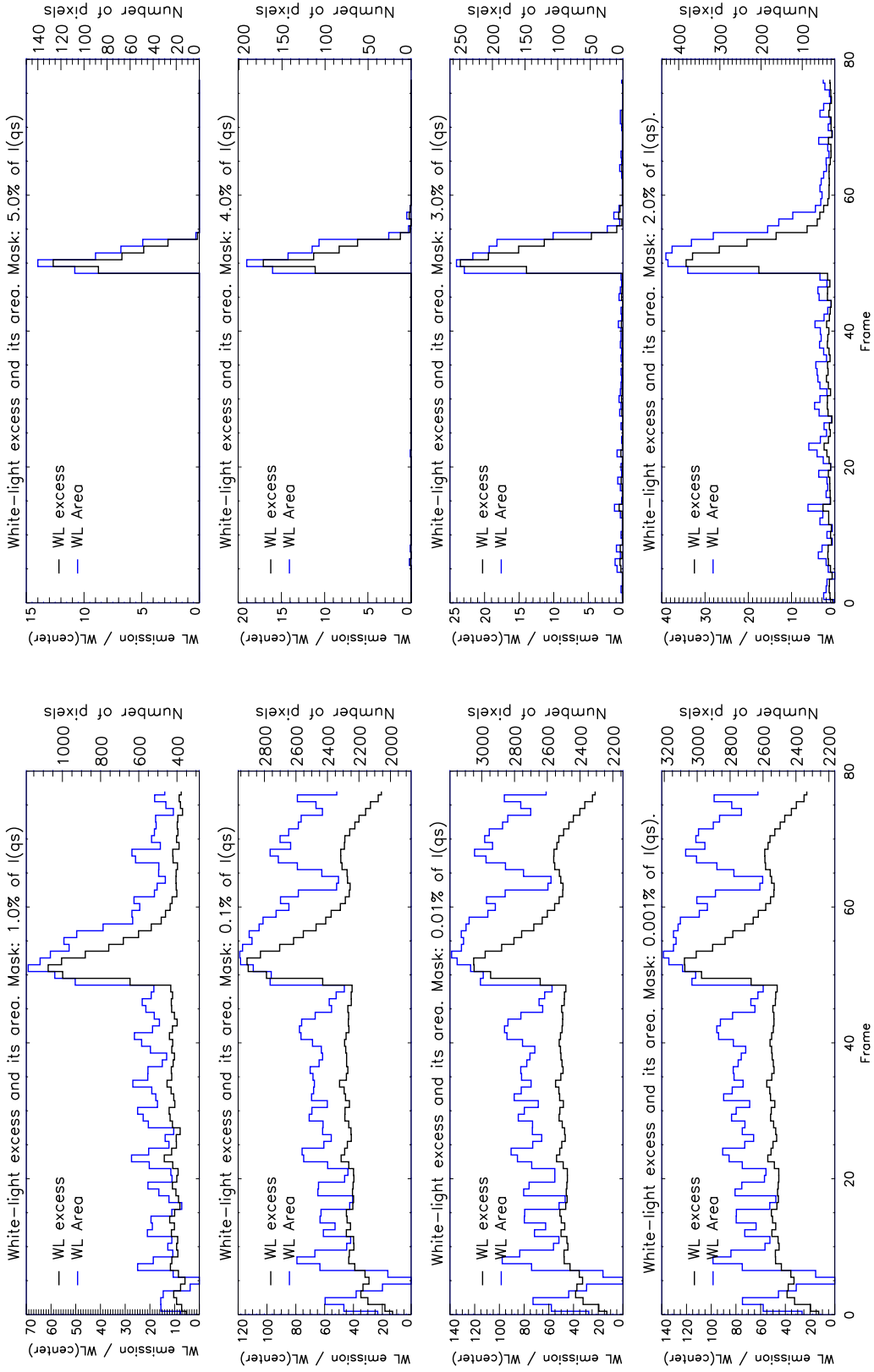


Figure 4.7: WL enhancement curve (blue line) and its area (black line) during flare SOL-2011-07-30T02:12.0. Flux was measured using the integration-differences, intensity and photometric masks. Each panel has a different value as zero level of mask which goes from 0.001 to 5.0 percentage of quiet-sun intensity.

Flare	Date	Start time	End time	Peak time	Goes Class	WL duration seconds	Conversion factor [DNs ⁻¹ W ⁻¹ m ²]
1.	Oct 16, 2010	19:07	19:15	19:12	M2.9	405	4.712E+08
2.	Feb 13, 2011	17:28	17:47	17:38	M6.6	270	4.749E+08
3.	Feb 15, 2011	01:44	02:06	01:56	X2.2	540	4.725E+08
4.	Feb 18, 2011	09:55	10:11	10:00	M6.6	495	4.723E+08
5.	Feb 18, 2011	12:59	13:06	13:00	M1.4	225	4.741E+08
6.	Feb 18, 2011	20:56	21:04	21:00	M1.3	450	4.718E+08
7.	Mar 07, 2011	19:43	20:12	20:01	M3.7	360	4.669E+08
8.	Mar 09, 2011	23:13	23:29	23:23	X1.5	360	4.657E+08
9.	Mar 14, 2011	19:30	19:52	19:38	M4.2	270	4.652E+08
10.	Mar 15, 2011	00:18	00:24	00:22	M1.0	360	4.642E+08
11.	Jul 30, 2011	02:04	02:12	02:09	M9.3	540	4.362E+08
12.	Sep 06, 2011	22:12	22:24	22:20	X2.1	495	4.393E+08
13.	Sep 08, 2011	15:32	15:52	15:46	M6.7	270	4.422E+08
14.	Sep 24, 2011	09:21	09:48	09:40	X1.9	450	4.421E+08
15.	Sep 24, 2011	20:29	20:42	20:30	M5.8	360	4.471E+08
16.	Dec 31, 2011	16:16	16:34	16:26	M1.5	405	4.546E+08
17.	May 06, 2012	01:12	01:20	01:18	M1.1	270	4.234E+08
18.	May 08, 2012	13:02	13:12	13:08	M1.4	360	4.254E+08
19.	May 10, 2012	04:11	04:23	04:18	M5.7	405	4.224E+08
20.	Jun 09, 2012	16:45	16:56	16:53	M1.8	495	4.178E+08
21.	Jun 29, 2012	09:13	09:22	09:20	M2.2	405	4.157E+08
22.	Jul 04, 2012	14:35	14:42	14:40	M1.3	405	4.156E+08
23.	Jul 04, 2012	09:47	09:57	09:55	M5.3	225	4.167E+08
24.	Jul 05, 2012	11:39	11:49	11:44	M6.1	315	4.141E+08
25.	Jul 05, 2012	03:25	03:39	03:36	M4.7	585	4.146E+08
26.	Jul 05, 2012	01:05	01:15	01:10	M2.4	540	4.164E+08
27.	Jul 06, 2012	08:17	08:27	08:23	M1.5	315	4.143E+08

Table 4.1: General information of 27 White-light flares observed on the current solar maximum. The WL emitting time was calculated as $N * 45sec$; where N is the number of frames with WL emission.

Flare	Integration method			Mean method		
	WL Intensity [W m ⁻² sr ⁻¹ Å ⁻¹]	WL area [(Mm) ²]	Total energy [Joules]	WL Intensity [W m ⁻² sr ⁻¹ Å ⁻¹]	WL area [(Mm) ²]	Total energy [Joules]
1.	1.2E-02 ± 8.1E-04	11.6	1.8E+13 ± 6.6 %	1.6E-02 ± 1.9E-03	28.1	5.8E+13 ± 11.5%
2.	2.3E-02 ± 9.7E-04	166.0	3.2E+14 ± 4.3 %	8.4E-02 ± 2.3E-03	945.9	6.7E+15 ± 2.8%
3.	6.5E-02 ± 9.9E-04	1510.9	1.7E+16 ± 1.5 %	2.8E-01 ± 2.5E-03	9829.2	4.6E+17 ± 0.9%
4.	3.9E-02 ± 1.5E-03	541.8	3.3E+15 ± 3.9 %	1.5E-01 ± 3.5E-03	2548.7	6.0E+16 ± 2.3%
5.	3.2E-03 ± 4.5E-04	4.7	1.1E+12 ± 14.1%	1.3E-02 ± 1.2E-03	39.3	3.7E+13 ± 8.8%
6.	2.0E-02 ± 5.3E-04	95.3	2.7E+14 ± 2.7 %	7.5E-02 ± 1.5E-03	885.3	9.4E+15 ± 2.0%
7.	5.6E-03 ± 8.5E-04	16.9	1.1E+13 ± 15.1%	3.0E-02 ± 2.0E-03	209.1	7.1E+14 ± 6.7%
8.	3.4E-02 ± 1.3E-03	432.0	1.6E+15 ± 4.0 %	1.2E-01 ± 3.2E-03	2415.0	3.3E+16 ± 2.6%
9.	8.8E-03 ± 5.7E-04	32.6	2.4E+13 ± 6.4 %	3.5E-02 ± 1.4E-03	234.8	6.9E+14 ± 4.0%
10.	6.2E-03 ± 6.4E-04	20.2	1.4E+13 ± 10.3%	3.5E-02 ± 1.6E-03	306.4	1.2E+15 ± 4.5%
11.	6.0E-02 ± 1.0E-03	375.3	3.8E+15 ± 1.7 %	1.3E-01 ± 2.6E-03	1526.0	3.3E+16 ± 2.0%
12.	7.1E-02 ± 9.3E-04	751.9	8.3E+01 ± 1.3 %	1.6E-01 ± 2.3E-03	2712.1	6.8E+16 ± 1.4%
13.	1.2E-02 ± 5.1E-04	42.5	4.2E+13 ± 4.4 %	4.6E-02 ± 1.3E-03	314.6	1.2E+15 ± 2.7%
14.	5.0E-03 ± 5.8E-04	5.9	4.1E+12 ± 11.7%	2.1E-02 ± 1.5E-03	115.9	3.5E+14 ± 7.2%
15.	3.3E-02 ± 5.5E-04	134.7	5.0E+14 ± 1.7 %	8.5E-02 ± 1.4E-03	992.4	9.5E+15 ± 1.7%
16.	7.8E-03 ± 1.1E-03	16.4	1.6E+13 ± 13.9%	3.2E-02 ± 2.5E-03	149.4	6.1E+14 ± 7.7%
17.	1.5E-03 ± 5.1E-04	0.9	1.1E+11 ± 33.8%	1.5E-02 ± 1.5E-03	74.4	9.7E+13 ± 10.1%
18.	5.6E-03 ± 1.0E-03	13.0	8.2E+12 ± 18.4%	2.8E-02 ± 2.5E-03	142.6	4.5E+14 ± 8.8%
19.	3.6E-02 ± 1.4E-03	395.9	1.8E+15 ± 3.8 %	1.2E-01 ± 3.2E-03	1772.8	2.6E+16 ± 2.8%
20.	3.2E-03 ± 6.8E-04	8.3	4.2E+12 ± 21.0%	4.2E-02 ± 2.0E-03	593.4	3.9E+15 ± 4.9%
21.	2.4E-02 ± 1.3E-03	158.8	4.8E+14 ± 5.7 %	7.1E-02 ± 3.0E-03	665.3	6.0E+15 ± 4.2%
22.	2.2E-02 ± 1.4E-03	82.7	2.3E+14 ± 6.2 %	6.2E-02 ± 3.2E-03	486.7	3.8E+15 ± 5.3%
23.	1.6E-02 ± 1.0E-03	101.4	1.2E+14 ± 6.3 %	6.6E-02 ± 2.5E-03	669.0	3.1E+15 ± 3.8%
24.	8.5E-03 ± 6.2E-04	29.9	2.5E+13 ± 7.3 %	4.5E-02 ± 1.6E-03	323.0	1.5E+15 ± 3.5%
25.	1.9E-02 ± 1.5E-03	34.1	1.2E+14 ± 7.8 %	6.9E-02 ± 3.7E-03	522.6	6.7E+15 ± 5.3%
26.	3.9E-02 ± 1.4E-03	357.6	2.4E+15 ± 3.6 %	1.6E-01 ± 3.5E-03	3026.8	8.2E+16 ± 2.2%
27.	8.0E-03 ± 1.0E-03	13.8	1.1E+13 ± 13.0%	2.9E-02 ± 2.6E-03	133.4	3.8E+14 ± 8.9%

Table 4.2: WL intensity at 6173 Å, its area and total energy emitted during 27 WLFs observed on the current solar maximum. From second to fourth columns presented the measurements using the integration reduction method, and from fifth to seventh columns were perform the mean reduction method.

CHAPTER
FIVE

BIBLIOGRAPHY

- Aboudarham, J., Henoux, J.C.: 1986, Energy deposit at temperature minimum level and white light flares. *A&A* **156**, 73–78. 9, 10, 17
- Allred, J.C., Hawley, S.L., Abbott, W.P., Carlsson: 2005, Radiative Hydrodynamic Models of the Optical and Ultraviolet Emission from Solar Flares. *ApJ* **630**, 573–586. doi:10.1086/431751. 9, 10
- Antonucci, E.: 1989, Solar flare spectral diagnosis - Present and future. *Sol. Phys.* **121**, 31–60. doi:10.1007/BF00161686. 8
- Athay, R.G., Moreton, G.E.: 1961, Impulsive Phenomena of the Solar Atmosphere. I. Some Optical Events Associated with Flares Showing Explosive Phase. *ApJ* **133**, 935. doi:10.1086/147098. 6
- Avrett, E.H., Loeser, R.: 1992, The PANDORA Atmosphere Program (Invited Review). In: Giampapa, M.S., Bookbinder, J.A. (eds.) *Cool Stars, Stellar Systems, and the Sun, Astronomical Society of the Pacific Conference Series* **26**, 489. 17
- Battaglia, M., Kontar, E.P.: 2011, Height structure of X-ray, EUV, and white-light emission in a solar flare. *A&A* **533**, L2. doi:10.1051/0004-6361/201117605. 8, 9
- Benz, A.: 2000, In: Murdin, P. (ed.) *Solar Flare Observations*. doi:10.1888/0333750888/2049. 6
- Benz, A.O.: 2008, Flare Observations. *Living Reviews in Solar Physics* **5**, 1. doi:10.12942/lrsp-2008-1. 5
- Bruno, R., Carbone, V.: 2013, The solar wind as a turbulence laboratory. *Living Reviews in Solar Physics* **10**(2). doi:10.12942/lrsp-2013-2. <http://www.livingreviews.org/lrsp-2013-2>. 3

-
- Bumba, V., Křivský, L.: 1959, Chromospheric pre-flares. *Bulletin of the Astronomical Institutes of Czechoslovakia* **10**, 221. 6
- Chandrasekhar, S., Chandrasekhar, S.: 1967, *An introduction to the study of stellar structure, Astrophysical monographs*, Dover Publications, ??? ISBN 9780486136288. 11
- Charbonneau, P.: 2010, Dynamo Models of the Solar Cycle. *Living Reviews in Solar Physics* **7**, 3. doi:10.12942/lrsp-2010-3. 2
- Cox, D.P., Tucker, W.H.: 1969, Ionization Equilibrium and Radiative Cooling of a Low-Density Plasma. *ApJ* **157**, 1157. doi:10.1086/150144. 17
- De Pontieu, B., Erdélyi, R., James, S.P.: 2004, Solar chromospheric spicules from the leakage of photospheric oscillations and flows. *Nature* **430**, 536–539. doi:10.1038/nature02749. 3
- de Pontieu, B., McIntosh, S., Hansteen, V.H., Carlsson, M., Schrijver, C.J., Tarbell, T.D., Title, A.M., Shine, R.A., Suematsu, Y., Tsuneta, S., Katsukawa, Y., Ichimoto, K., Shimizu, T., Nagata, S.: 2007, A Tale of Two Spicules: The Impact of Spicules on the Magnetic Chromosphere. *PASJ* **59**, 655. 3
- Ding, M.D., Fang, C., Yun, H.S.: 1999, Heating in the Lower Atmosphere and the Continuum Emission of Solar White-Light Flares. *ApJ* **512**, 454–457. doi:10.1086/306776. 8
- Donnelly, R.F.: 1976, Empirical models of solar flare X ray and EUV emission for use in studying their E and F region effects. *J. Geophys. Res.* **81**, 4745–4753. doi:10.1029/JA081i025p04745. 9, 18
- Doughty, N.A., Fraser, P.A.: 1966, The free-free absorption coefficient of the negative hydrogen ion. *MNRAS* **132**, 267. 20
- Doughty, N.A., Fraser, P.A., McEachran, R.P.: 1966, The bound-free absorption coefficient of the negative hydrogen ion. *MNRAS* **132**, 255. 20
- Emerson, D.: 1996, *Interpreting astronomical spectra*, John Wiley & Sons, ??? ISBN 9780471976790. 11, 13
- Fang, C., Ding, M.D.: 1995, On the spectral characteristics and atmospheric models of two types of white-light flares. *A&AS* **110**, 99. 8
- Fletcher, L., Hannah, I.G., Hudson, H.S., Metcalf, T.R.: 2007, A TRACE White Light and RHESSI Hard X-Ray Study of Flare Energetics. *ApJ* **656**, 1187–1196. doi:10.1086/510446. 8, 9

Gebbie, K.B., Thomas, R.N.: 1970, On the Dependence of $T_{\{e\}}$ upon Quantity Versus Quality of the Radiation Field in a Stellar Atmosphere. *ApJ* **161**, 229. doi:10.1086/150527. 20

Gnedin, N.Y., Hollon, N.: 2012, Cooling and Heating Functions of Photoionized Gas. *ApJS* **202**, 13. doi:10.1088/0067-0049/202/2/13. 16

Hale, G.E., Ellerman, F.: 1904, Calcium and Hydrogen Flocculi. *ApJ* **19**, 41. doi:10.1086/141083. 3

Hansen, C.J., Kawaler, S.D., Trimble, V.: 2004, *Stellar interiors: Physical principles, structure, and evolution, Astronomy and Astrophysics Library*, Springer New York, ??? ISBN 9780387200897. <http://books.google.com.co/books?id=NnBq7R0M4UgC>. 20

Hiei, E., Nakagomi, Y., Takuma, H.: 1992, White-light flare observed at the solar limb. *PASJ* **44**, 55–62. 20

Hudson, H.S.: 1972, Thick Target Processes and White Light Flares. *Sol. Phys.* **24**, 414–428. doi:10.1007/BF00153384. 9, 10

Hudson, H.S., Wolfson, C.J., Metcalf, T.R.: 2006, White-Light Flares: A TRACE/RHESSI Overview. *Sol. Phys.* **234**, 79–93. doi:10.1007/s11207-006-0056-y. 8, 49

Hudson, H.S., Acton, L.W., Hirayama, T., Uchida, Y.: 1992, White-light flares observed by YOHKOH. *PASJ* **44**, 77–81. 8, 9, 36

Hughes, D.W., Rosner, R., Weiss, N.: 2007, *The solar tachocline*, Cambridge University Press, ??? ISBN 9781139462587. <http://books.google.com.co/books?id=1WD5xUp8fWIC>. 2

Jess, D.B., Mathioudakis, M., Crockett, P.J., Keenan, F.P.: 2008, Do All Flares Have White-Light Emission? *ApJL* **688**, 119–122. doi:10.1086/595588. 10, 45, 48, 49

Kane, S.R., Donnelly, R.F.: 1971, Impulsive Hard X-Ray and Ultraviolet Emission during Solar Flares. *ApJ* **164**, 151. doi:10.1086/150826. 6

Karttunen, H., Kröger, P., Oja, H., Donner, K.J., Poutanen, M.: 2007, *Fundamental astronomy*, Springer, ??? ISBN 9783540341444. <http://books.google.com.co/books?id=DjeVdb0sLEAC>. 2

Kerr, G.S., Fletcher, L.: 2014, Physical Properties of White-Light Sources in the 2011 Feb 15 Solar Flare. *ArXiv e-prints*. 47, 48

-
- Kramida, A., Yu. Ralchenko, Reader, J., and NIST ASD Team: 2013,, NIST Atomic Spectra Database (ver. 5.1), [Online]. Available: <http://physics.nist.gov/asd> [2014, January 11]. National Institute of Standards and Technology, Gaithersburg, MD.. 23
- Machado, M.E., Emslie, A.G., Avrett, E.H.: 1989, Radiative backwarming in white-light flares. *Sol. Phys.* **124**, 303 – 317. doi:10.1007/BF00156272. III, VI, 9, 10, 15, 16, 17, 18, 19, 42, 49
- Machado, M.E., Emslie, A.G., Brown, J.C.: 1978, The structure of the temperature minimum region in solar flares and its significance for flare heating mechanisms. *Sol. Phys.* **58**, 363 – 387. doi:10.1007/BF00157282. VIII, 15, 43, 49
- Machado, M.E., Avrett, E.H., Vernazza, J.E., Noyes, R.W.: 1980, Semiempirical models of chromospheric flare regions. *ApJ* **242**, 336 – 351. doi:10.1086/158467. III, 15, 16, 17, 19
- Machado, M.E., Avrett, E.H., Falciani, R., Fang, C., Gesztesy, L., Henoux, J.-C., Hiei, E., Neidig, D.F., Rust, D.M., Sotirovski, P., Svestka, Z., Zirin, H.: 1986, White light flares and atmospheric modeling (Working Group report). In: Neidig, D.F. (ed.) *The lower atmosphere of solar flares*, p. 483 - 488, 483 – 488. 8
- Martínez Oliveros, J.C., Couvidat, S., Schou, J., Krucker, S., Lindsey, C., Hudson, H.S., Scherrer, P.: 2011, Imaging Spectroscopy of a White-Light Solar Flare. *Sol. Phys.* **269**, 269 – 281. doi:10.1007/s11207-010-9696-z. 9, 36
- Martínez Oliveros, J.-C., Hudson, H.S., Hurford, G.J., Krucker, S., Lin, R.P., Lindsey, C., Couvidat, S., Schou, J., Thompson, W.T.: 2012, The Height of a White-light Flare and Its Hard X-Ray Sources. *ApJL* **753**, L26. doi:10.1088/2041-8205/753/2/L26. 8
- Matthews, S.A., van Driel-Gesztelyi, L., Hudson, H.S., Nitta, N.V.: 2003, A catalogue of white-light flares observed by Yohkoh. *A&A* **409**, 1107 – 1125. doi:10.1051/0004-6361:20031187. 8, 9, 36
- Metcalf, T.R., Alexander, D., Hudson, H.S., Longcope, D.W.: 2003, TRACE and Yohkoh Observations of a White-Light Flare. *ApJ* **595**, 483 – 492. doi:10.1086/377217. 8, 9, 45, 46
- Miesch, M.S.: 2005, Large-Scale Dynamics of the Convection Zone and Tachocline. *Living Reviews in Solar Physics* **2**, 1. doi:10.12942/lrsp-2005-1. 2
- Najita, K., Orrall, F.Q.: 1970, White Light Events as Photospheric Flares. *Sol. Phys.* **15**, 176 – 194. doi:10.1007/BF00149484. 10, 18

-
- Neidig, D.F., Kane, S.R.: 1993, Energetics and timing of the hard and soft X-ray emissions in white light flares. *Sol. Phys.* **143**, 201 – 204. doi:10.1007/BF00619106. 8
- Potts, H., Hudson, H., Fletcher, L., Diver, D.: 2010, The Optical Depth of White-light Flare Continuum. *ApJ* **722**, 1514 – 1521. doi:10.1088/0004-637X/722/2/1514. 45
- Pulkkinen, T.: 2007, Space weather: Terrestrial perspective. *Living Reviews in Solar Physics* **4**(1). doi:10.12942/lrsp-2007-1. <http://www.livingreviews.org/lrsp-2007-1>. 3
- Richardson, R.S.: 1944, Solar Flares Versus Bright Chromospheric Eruptions : A Question of Terminology. *PASP* **56**, 156. doi:10.1086/125638. 5
- Rogers, F.J., Iglesias, C.A.: 1994, Astrophysical Opacity. *Science* **263**, 50 – 55. doi:10.1126/science.263.5143.50. 11
- Rust, D.M.: 1986, On the causes of white-light flares. In: Neidig, D.F. (ed.) *The lower atmosphere of solar flares; Proceedings of the Solar Maximum Mission Symposium, Sunspot, NM, Aug. 20-24, 1985 (A87-26201 10-92)*. Sunspot, NM, National Solar Observatory, 1986, p. 282-296., 282 – 296. 9
- Rutten, R.J.: 2003, *Radiative Transfer in Stellar Atmospheres*. 14, 20
- Solanki, S.K.: 2003, Sunspots: An overview. *A&A Rev.* **11**, 153 – 286. doi:10.1007/s00159-003-0018-4. 3
- Stilley, J.L., Callaway, J.: 1970, Free-Free Absorption Coefficient of the Negative Hydrogen Ion. *ApJ* **160**, 245. doi:10.1086/150423. 20
- Thomas, G.B., Finney, R.L.: 1996, *Calculus and analytic geometry, Calculus and Analytic Geometry pt. 1*, Addison-Wesley, ??? ISBN 9780201531749. <http://books.google.com.co/books?id=b3kZAQAAIAAJ>. 38
- Unsold, A.: 1968, On the Theory of Flares and Some Related Solar Phenomena. *QJRAS* **9**, 294. 10
- Vernazza, J.E., Avrett, E.H., Loeser, R.: 1973, Structure of the solar chromosphere. Basic Computations and Summary of the Results. *ApJ* **184**, 605 – 632. doi:10.1086/152353. VI, 14, 16, 19, 43
- Vernazza, J.E., Avrett, E.H., Loeser, R.: 1976, Structure of the solar chromosphere. II - The underlying photosphere and temperature-minimum region. *ApJS* **30**, 1 – 60. doi:10.1086/190356. VI, 16, 19, 20, 21, 22, 23, 43

-
- Vernazza, J.E., Avrett, E.H., Loeser, R.: 1981, Structure of the solar chromosphere. III - Models of the EUV brightness components of the quiet-sun. *ApJS* **45**, 635–725. doi:10.1086/190731. VI, VIII, 16, 19, 21, 23, 43
- Wiese, W.L., Fuhr, J.R.: 2009, Accurate atomic transition probabilities for hydrogen, helium, and lithium. *Journal of Physical and Chemical Reference Data* **38**(3), 565–720. doi:<http://dx.doi.org/10.1063/1.3077727>. <http://scitation.aip.org/content/aip/journal/jpcrd/38/3/10.1063/1.3077727>. 23
- Zharkova, V.V., Kobylinskii, V.A.: 1993, The effect of non-thermal excitation and ionization on the hydrogen emission in impulsive solar flares. *Sol. Phys.* **143**, 259–274. doi:10.1007/BF00646487. 10
- Zirin, H.: 1966, *The solar atmosphere*. 2

APPENDIX
A

ATTENDED CONFERENCES, PAPERS & POSTERS.

In this appendix are listed the participations on meetings and other results during my undergraduate studies.

(I) Paper in preparation.

Statistical Characterization of Solar White - Light Flares Detected in the Current Solar Cycle.

J. S. Castellanos-Durán, J. D. Alvarado-Gómez, W. Fajardo
J.C. Martínez Oliveros & B. Calvo-Mozo.

(II) Poster.

Cluster analysis for two solar physics problems: Stokes parameters & NUV spectra.

J. S. Castellanos-Durán & L. Kleint.

The 2013 IRIS Student Summer Intern Research Program. Lockheed Martin Solar and Astrophysics Laboratory and Stanford University, Palo Alto - CA, USA. 2013.

(III) Contributed Talk.

Characterization of white light, SXR and HXR kernels emissions in white light flares observed by SDO/HMI and RHESSI.

J.S. Castellanos-Durán, J.D. Alvarado-Gómez & B. Calvo-Mozo.

12th RHESSI Workshop: Solar in Sonoma. Tracing the Connections in Solar Eruptive Events. University of California, Berkeley - NASA, Petaluma - CA, USA. 2012.

(IV) Poster.

Characterization of white light, SXR and HXR kernels emissions in white light flares observed by SDO/HMI and RHESSI.

J.S. Castellanos-Durán, J.D. Alvarado-Gómez & B.

Calvo-Mozo.

American Geophysical Union (AGU) fall meeting, San Francisco - CA, USA.

(V) Contributed Talk and proceedings.

Caracterización de la emisión en luz blanca y en rayos-X de la fulguración GOES M6.6 del 18 de Febrero de 2011 usando SDO y RHESSI.

J.S. Castellanos-Durán, J.D. Alvarado-Gómez & B. Calvo-Mozo.

Encuentro Nacional de investigación y desarrollo National¹ ENID 2012. Universidad Nacional de Colombia, Bogotá, Colombia. 2012.

(VI) Poster.

Study of the white light and hard X-rays emission of the M6.6 class flare of February 18 2011 using SDO/HMI and RHESSI.

J. S. Castellanos-Durán, J. D. Alvarado-Goméz, J.C. Martínez Oliveros & B. Calvo-Mozo.

International Summer School in Solar Astrophysics: Modern Trends and Techniques. Universidad Nacional de Colombia, Bogotá, Colombia. 2012.

(VII) Poster.

Observational Analysis of Photospheric Magnetic Field Restructuring During Energetic Solar Flares .

J.D. Alvarado, J.S. Castellanos, J.C. Buitrago, J.C. Martínez, C.Lindsey, W.P. Abbott & G.H. Fisher.

American Geophysical Union (AGU) fall meeting, San Francisco - CA, USA. 2011.

Following there is a copy of the paper in preparation (I), the proceeding (V) and the posters (II, IV, VI VII) listed below.

¹National meeting in research and development.